Wind-induced changes to shoaling surface gravity wave shape

Thomas J. Zdyrski and Falk Feddersen

(Received xx; revised xx; accepted xx)

Unforced shoaling waves experience growth and changes to wave shape. Similarly, wind-forced waves on a flat-bottom likewise experience growth/decay and changes to wave shape. However, the combination of shoaling and wind-forcing, particularly relevant in the near shore environment, has rarely been investigated. Here, we consider small-amplitude, shallow-water solitary waves propagating up a gentle, planar bathymetry forced by a weak, Jeffreys-type wind-induced surface pressure. We derive a variable-coefficient Korteweg–de Vries–Burgers (vKdV–B) equation governing the surface profile's evolution and solve it numerically using a Runge-Kutta third-order finite difference solver. The simulations run until convective pre-breaking—a Froude number limit appropriate to the order of the vKdV–B. Offshore winds weakly enhance the ratio of pre-breaking height to depth as well as pre-breaking slope. Onshore winds have a strong impact on narrowing the wave peak, and wind also modulates the rear shelf formed behind the wave. Furthermore, wind strongly affects the width of the pre-breaking zone, with larger effects for smaller beach slopes. After converting our pressure magnitudes to physically realistic wind speeds, we observe qualitative agreement with prior laboratory and numerical experiments. Finally, we isolate the wind's effect by comparing the wave profiles to the unforced case. This reveals that the numerical results are approximately a superposition of a solitary wave, a shoaling-induced shelf and a wind-induced, bound, dispersive and decaying tail.

Key words: surface gravity waves, wind-wave interactions, solitary waves

1. Introduction

Wind coupled to surface gravity waves leads to wave growth and decay as well as changes to wave shape. However, many aspects of wind-wave coupling are not yet fully understood. Since the sheltering theory of wind-wave coupling by Jeffreys (1925), a variety of mechanisms for wind-wave interactions have been put forward, often with a focus on calculating growth rates (*e.g.*, Miles 1957; Phillips 1957). Furthermore, these theories have been tested by many studies in the laboratory (*e.g.*, Wu 1968; Phillips & Banner 1974; Plant & Wright 1977; Buckley & Veron 2019) and the field (*e.g.*, Hasselmann *et al.* 1973; Donelan *et al.* 2006). Similarly, numerical studies have modeled the airflow above waves using methods such as large eddy simulations (*e.g.*, Hara & Sullivan 2015; Yang *et al.* 2013; Husain *et al.* 2019) or modeled the combined air and water domain using Reynolds-averaged Navier Stokes (RANS) solvers (*e.g.*, Zou & Chen 2017) or direct numerical simulations (*e.g.*, Zonta *et al.* 2015; Yang *et al.* 2018).

While wave growth rates and airflow structure have received much attention, wind-induced wave shape changes have been less studied. Unforced, weakly nonlinear waves on flat bottoms (*e.g.* Stokes, cnoidal, and solitary waves) are horizontally symmetric about the peak (*i.e.* zero asymmetry) but are not vertically symmetric (*i.e.* non-zero skewness, *e.g.*, Amick & Toland 1981; Toland 1999). Laboratory experiments of wind blowing over periodic waves have demonstrated that wave asymmetry increases with onshore wind speed in intermediate-water (*e.g.*, Leykin *et al.* 1995) and deep-water (*e.g.*, Feddersen & Veron 2005). Theoretical studies have likewise shown that wind-induced surface pressure induces wave shape changes in both deep (Zdyrski & Feddersen 2020) and shallow (Zdyrski & Feddersen 2021) water. However, the influence of wind on wave shape has not yet been investigated theoretically for shoaling waves on a sloping bottom.

In contrast, the shoaling of unforced waves up a beach is a relatively well-studied phenomenon that causes wave growth and shape change. Field observations have revealed the importance of nonlinearity in wave shoaling and its relation to skewness and asymmetry (*e.g.*, Elgar & Guza 1985; Freilich & Guza 1984). Additionally, laboratory experiments of waves shoaling on planar beach slopes yield how the wave height and wave shape evolve with distance up the beach (*e.g.*, Zelt 1991; Beji & Battjes 1993; Grilli *et al.* 1994). Furthermore, numerical studies have investigated wave shoaling all the way to wave breaking. A variety of methods have been utilized, including pseudo-spectral models (*e.g.*, Knowles & Yeh 2018), fully nonlinear potential flow boundary element method solvers (*e.g.*, Grilli *et al.* 1997; Derakhti *et al.* 2020), large eddy simulation volume of fluid methods (*e.g.*, Derakhti *et al.* 2020) and two-phase direct numerical simulations of both the air and water (*e.g.*, Mostert & Deike 2020). Theoretical (*e.g.*, Brun & Kalisch 2018) and numerical (*e.g.*, Derakhti *et al.* 2020) investigations of wave breaking have shown that convective wave breaking depends on the surface water velocity u and the phase speed c and occurs when the Froude number $\mathrm{Fr} \coloneqq u/c$ is approximately unity. The type of wave breaking (*e.g.* spilling, plunging, surging, *etc.*) is related to the beach slope β, initial wave height H_0 and initial wave width L_0 through the Iribarren number $\mathrm{Ir} \coloneqq \beta/\sqrt{H_0/L_0}$ (*e.g.*, Iribarren 1949; Lara *et al.* 2011).

There have been extremely few studies looking at the combined effects of wind and shoaling of surface gravity waves. Experimental studies have found that onshore wind increases the surf zone width (*e.g.*, Douglass 1990) and decreases the wave height-to-water depth ratio at breaking (*e.g.*, King & Baker 1996), with offshore wind having the opposite effect. Additionally, numerical studies using two-phase RANS solvers of wind-forced solitary (*e.g.*, Xie 2014) and periodic (*e.g.*, Xie 2017) breaking waves have demonstrated that increasingly onshore winds enhance the wave height at all points prior to breaking. Furthermore, only Feddersen & Veron (2005) and O'Dea *et al.* (2021) have investigated the combined influence of wind and shoaling on wave shape. Feddersen & Veron (2005) demonstrated that onshore winds enhance the shoaling-induced time-asymmetry. Cross-shore wind was weakly correlated to the void aspect ratio of strongly-nonlinear, plunging waves with offshore (onshore) wind reducing (increasing) the aspect ratio (O'Dea *et al.* 2021), although the wind-variation was relatively weak. Nevertheless, a theoretical description of wind-induced changes to wave shoaling (*e.g.* wave shape, breaking location, *etc.*) has not yet been developed.

Therefore, this study will derive a simplified, theoretical model for wind-forced shoaling waves that takes the form of a variable-coefficient Korteweg–de Vries (KdV)–Burgers equation. The standard KdV equation describes unidirectional wave propagation with weak nonlinearity and dispersion in shallow, flat-bottomed domains (*e.g.*, Hammack & Segur 1974). It has localized solutions, known as solitary waves, which propagate without changing shape by balancing nonlinearity and dispersion (*e.g.*, Mei *et al.* 2005). Furthermore, arbitrary initial conditions will decay into a number of discrete solitary waves as well as an oscillatory, dispersive tail (*e.g.*, Hammack & Segur 1974). When the bottom bathymetry is allowed to vary, the coefficients of the KdV equation are no longer constant and the system is described by a variable-coefficient KdV (vKdV) equation (*e.g.*, Johnson 1973; Svendsen & Hansen 1978). The deformation of solitary waves propagating on a sloping-bottom vKdV system has been studied both analytically (*e.g.*, Miles 1979) and numerically (*e.g.*, Knowles & Yeh 2018) with solitary wave initial conditions becoming deformed and gaining a rear "shelf" for small enough slopes (*e.g.*, Miles 1979). Alternatively, if the flat-bottomed KdV equation is augmented with a wind-induced surface pressure forcing, the KdV–Burgers (KdV–B) equation results (Zdyrski & Feddersen 2020). Wind in the KdV–B equation induces a solitary-wave initial condition to continuously generate a bound, dispersive and decaying tail with polarity depending on the wind direction (Zdyrski & Feddersen 2020), analogous to a KdV non-solitary-wave initial condition (*e.g.*, Newell 1985).

Here, we apply a wind-induced pressure forcing over a sloping bathymetry to derive a vKdV–Burgers equation and determine a convective pre-breaking condition in § 2. We then solve the resulting vKdV–Burgers equation numerically using a third-order Runge-Kutta solver and investigate the changes to wave shape and pre-breaking location in § 3. Finally, we examine the relationship between pressure and wind speed, isolate the effect of wind from the effect of shoaling, and discuss how our findings relate to previous laboratory and numerical studies in § 4.

2. vKdV–Burgers equation derivation and model setup

2.1. *Governing equations*

We derive a vKdV–Burgers equation for wind-forced shoaling waves by considering incompressible, irrotational, inviscid flows and neglecting surface tension. We restrict our attention to planar, two-dimensional waves propagating in the $+x$-direction. Additionally, we choose the $+z$-direction to be vertically upwards with the $z = 0$ datum at the mean water level and impose a bottom bathymetry at $z = -h(x)$. The standard incompressibility, bottom boundary, kinematic boundary and dynamic boundary conditions are

$$0 = \frac{\partial^2 \phi}{\partial x^2} + \frac{\partial^2 \phi}{\partial z^2} \qquad \text{on} \quad -h < z < \eta\,, \tag{2.1}$$

$$\frac{\partial \phi}{\partial z} = -\frac{\partial h}{\partial x}\frac{\partial \phi}{\partial x} \qquad \text{on} \quad z = -h, \tag{2.2}$$

$$\frac{\partial \phi}{\partial z} = \frac{\partial \eta}{\partial t} + \frac{\partial \phi}{\partial x}\frac{\partial \eta}{\partial x} \qquad \text{on} \quad z = \eta\,, \tag{2.3}$$

$$0 = \frac{p}{\rho_w} + g\eta + \frac{\partial \phi}{\partial t} + \frac{1}{2}\left[\left(\frac{\partial \phi}{\partial x}\right)^2 + \left(\frac{\partial \phi}{\partial z}\right)^2\right] \quad \text{on} \quad z = \eta\,. \tag{2.4}$$

We have introduced the wave profile $\eta(x,t)$, the velocity potential $\phi(x,z,t)$ derived from the water velocity $\mathbf{u} = \boldsymbol{\nabla}\phi$, the surface pressure $p(x,t)$, the gravitational acceleration g and the water density ρ_w which is much larger than the air density $\rho_a \approx 1.225 \times 10^{-3}\rho_w$. Additionally, we removed the Bernoulli constant from the dynamic boundary condition by using the ϕ gauge freedom. Next, to examine the wind's effect on shoaling waves, we impose the analytically-simple Jeffreys-type surface pressure $p(x,t)$ forcing (Jeffreys 1925):

$$p(x,t) = P\frac{\partial \eta(x,t)}{\partial x}\,. \tag{2.5}$$

The pressure constant $P \propto \rho_a(U-c)^2$ depends on the wave phase speed c and wind speed U (*cf.* § 4.1). For a wave propagating towards the shore, onshore winds yield $P > 0$ while offshore winds give $P < 0$. The application of a Jeffreys-type forcing to the flat-bottom KdV equation was discussed in Zdyrski & Feddersen (2021).

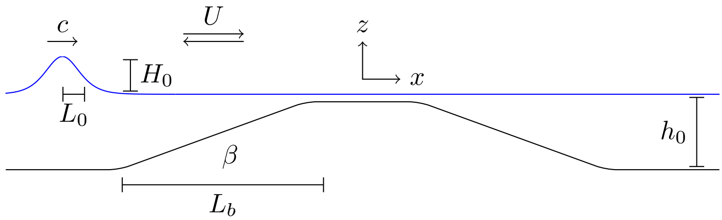

Figure 1. Schematic showing the (periodic) simulation domain and relevant length scales. The blue line represents the water surface and wave profile η, and the solid black line is the bottom bathymetry $h(x)$. The solitary wave initial condition has an effective half-width L_0 and height H_0 and begins with its peak on the far left side, in the middle of flat region of depth h_0. The initial wave then propagates to the right with phase speed c up the beach with slope β until it reaches pre-breaking (*cf.* § 2.6). The positive/negative wind speed U corresponds to an onshore/offshore wind forcing.

2.2. *Model domain and model parameters*

The model domain (figure 1) consists of an initial flat section 20 units long at a depth of $h_0 = 1$ and transitions smoothly at $x = 0$ into a planar beach region with constant slope β and characteristic beach width $L_b := h_0/\beta$, as defined by Knowles & Yeh (2018). The bathymetry then smoothly transitions to a flat plateau 40 units long at a depth of $h = 0.1$ followed by a downward slope with slope $-\beta$. Finally, there is another flat section at a depth of $h_0 = 1$ before the domain wraps periodically.

The initial condition will be a KdV solitary wave with height H_0 and width L_0 following Knowles & Yeh (2018), and L_0 will be specified later. The solitary wave begins centered on the left boundary, in between the two flat, deep, 20 unit-long sections. From the defined dimensional quantities, we specify four non-dimensional parameters,

$$\varepsilon_0 := \frac{H_0}{h_0}, \qquad \mu_0 := \left(\frac{h_0}{L_0}\right)^2, \qquad P_0 := \frac{P}{\rho_w g L_0}, \qquad \gamma_0 := \frac{L_0}{L_b}. \tag{2.5a–d}$$

Here, ε_0 is the non-dimensional initial wave height, μ_0 is the square reciprocal of the non-dimensional initial wave width, P_0 is the non-dimensional pressure magnitude (normalized by the initial wave width), and γ_0 is ratio of the initial wave width to the beach width. Note that the wave width-to-beach width ratio γ_0 is related to the beach slope β as $\gamma_0 = \beta/\sqrt{\mu_0}$. Together, these four non-dimensional parameters control the system's dynamics.

2.3. *Non-dimensionalization*

We non-dimensionalize our system's variables using the characteristic scales described in § 2.2: the initial depth h_0; the initial wave's height H_0; the initial wave's horizontal length scale L_0; the gravitational acceleration g; and the pressure magnitude P. Using primes for non-dimensional variables, we normalize as Zdyrski & Feddersen (2021) did and define

$$
\begin{aligned}
x &= L_0 x' = h_0 \frac{x'}{\sqrt{\mu_0}}\,, & h &= h' h_0\,,\\
z &= h_0 z'\,, & \eta &= H_0 \eta' = h_0 \varepsilon_0 \eta'\,,\\
t &= \frac{t' L_0}{\sqrt{g h_0}} = \frac{t'}{\sqrt{\mu_0}}\sqrt{\frac{h_0}{g}}\,, & \phi &= \phi' H_0 L_0 \sqrt{\frac{g}{h_0}} = \frac{\phi' \varepsilon_0}{\sqrt{\mu_0}}\sqrt{g h_0^3}\,.
\end{aligned}
\tag{2.6}
$$

We later assume the non-dimensional parameters ε_0, μ_0, γ_0 and P_0 are small to leverage a perturbative analysis. For the constant slope β beach profile, the spatial derivative of the bathymetry is also small $\partial_{x'} h' = \beta/\sqrt{\mu_0} = \gamma_0 \ll 1$ (the factor of $\sqrt{\mu_0}$ comes from the different non-dimensionalizations of h and x). However, perturbation analyses is simplest when all non-dimensional variables are $\mathcal{O}(1)$. Therefore, we leverage the two, horizontal length scales L_0 and L_b (*cf.* § 2.2) to define a non-dimensional, stretched bathymetry $\tilde{h}'$ that depends on $x/L_b = \gamma_0 x'$ as $\tilde{h}'(\gamma_0 x') = h'(x')$. Then, denoting derivatives with respect to $\gamma_0 x'$ using an overdot, the derivative of $\tilde{h}$ is $\dot{\tilde{h}}' := \partial_{\gamma_0 x'} \tilde{h}'(\gamma_0 x') = \mathcal{O}(1)$, and the small slope becomes explicit as $\partial_{x'} h' = \gamma_0 \dot{\tilde{h}}'$.

Now, the non-dimensional equations take the form

$$
0 = \mu_0 \frac{\partial^2 \phi'}{\partial x'^2} + \frac{\partial^2 \phi'}{\partial z'^2} \qquad \text{on} \quad -1 < z' < \varepsilon_0 \eta'\,, \tag{2.7}
$$

$$
\frac{\partial \phi'}{\partial z'} = -\mu_0 \gamma_0 \dot{\tilde{h}}' \frac{\partial \phi'}{\partial x'} \qquad \text{on} \quad z' = -\tilde{h}'(\gamma_0 x')\,, \tag{2.8}
$$

$$
\frac{\partial \phi'}{\partial z'} = \mu_0 \frac{\partial \eta'}{\partial t'} + \varepsilon_0 \mu_0 \frac{\partial \phi'}{\partial x'} \frac{\partial \eta'}{\partial x'} \qquad \text{on} \quad z' = \varepsilon_0 \eta'\,, \tag{2.9}
$$

$$
0 = P_0 \frac{\partial \eta'}{\partial x'} + \eta' + \frac{\partial \phi'}{\partial t'} + \frac{1}{2}\left[\varepsilon_0 \left(\frac{\partial \phi'}{\partial x'}\right)^2 + \frac{\varepsilon_0}{\mu_0}\left(\frac{\partial \phi'}{\partial z'}\right)^2\right] \qquad \text{on} \quad z' = \varepsilon_0 \eta'\,. \tag{2.10}
$$

For the remainder of § 2, we remove the primes for clarity.

2.4. *Boussinesq equations, multiple-scale expansion and vKdV–Burgers equation*

We follow the conventional Boussinesq equation derivation presented in, *e.g.*, Mei *et al.* (2005) or Ablowitz (2011). The two modifications we include are the weakly sloping bottom, similar to the treatment in Johnson (1973) and Mei *et al.* (2005), and the inclusion of a pressure forcing like that of Zdyrski & Feddersen (2021). For the sake of brevity, we only detail the relevant differences here. First, we expand the velocity potential in a Taylor series about the bottom $z = -h(x)$ as

$$
\phi(x, z, t) = \sum_{n=0}^{\infty} \left[z + \tilde{h}(\gamma_0 x)\right]^n \phi_n(x, t)\,. \tag{2.11}
$$

Substituting this expansion into the incompressibility equation (2.7) and bottom boundary condition (2.8) and assuming $\mu_0 \ll 1$ gives ϕ as a function of the velocity potential evaluated at the bottom $\varphi := \phi_0$. If we further assume that the bottom is very weakly sloping $\gamma_0 \sim \mu_0 \ll 1$, this simplifies to

$$
\phi = \varphi - \mu_0 \frac{1}{2}(z + \tilde{h})^2 \partial_x^2 \varphi + \mathcal{O}\left(\mu_0^2, \gamma_0^2, \gamma_0 \mu_0\right). \tag{2.12}
$$

Note that the assumption $\gamma_0 \sim \mu_0 \ll 1$ implies a moderate slope $\beta = \gamma_0 \sqrt{\mu_0} \sim \mu_0^{3/2}$ and is used by several other authors (*e.g.*, Johnson 1973; Miles 1979; Knowles & Yeh 2018).

For reference, if $\mu_0 = \gamma_0 = 0.1$, then this implies a physically realistic $\beta = 0.03$. Svendsen & Hansen (1978) compares this moderate slope to other theoretical derivations using larger or smaller slopes.

Substituting this ϕ expansion (2.12) into the kinematic and dynamic boundary conditions (2.9) and (2.10) yields Boussinesq-type equations with a pressure forcing term,

$$\partial_t\eta + \left(\tilde{h} + \varepsilon_0\eta\right)\partial_x^2\varphi \; + \left(\gamma_0\dot{\tilde{h}} + \varepsilon_0\partial_x\eta\right)\partial_x\varphi - \mu_0\frac{1}{6}\tilde{h}^3\partial_x^4\varphi = \mathcal{O}\left(\mu_0^2, \gamma_0^2, \gamma_0\mu_0\right), \tag{2.13}$$

$$P_0\partial_x\eta + \eta + \partial_t\varphi - \frac{1}{2}\mu_0\tilde{h}^2\partial_x^2\partial_t\varphi + \frac{1}{2}\varepsilon_0(\partial_x\varphi)^2 = \mathcal{O}\left(\mu_0^2, \gamma_0^2, \gamma_0\mu_0\right). \tag{2.14}$$

Note that replacing $\tilde{h}$ with the total depth $h_{\text{total}} = \tilde{h} + \varepsilon_0\eta$ shows that these are equivalent to the flat-bottomed Boussinesq equations with $h_{\text{total}} = 1 + \varepsilon_0\eta$. In other words, any sloping-bottom terms $\dot{\tilde{h}}$ only appear in the combination $\partial_x h_{\text{total}} = \gamma_0\dot{\tilde{h}} + \varepsilon_0\partial_x\eta$. This is expected since the only sloping-bottom term $\mu_0\gamma_0\dot{\tilde{h}}\partial_x\phi$ in the governing equations (2.7)–(2.10) was dropped when we neglected terms of $\mathcal{O}\left(\mu_0^2, \gamma_0^2, \gamma_0\mu_0\right)$.

Since the bathymetry varies on the slow scale x/γ_0, we expand our system in multiple spatial scales $x_n = \gamma_0^n x$ for $n = 0, 1, 2, \ldots$, so the derivatives become

$$\frac{\partial}{\partial x} \to \frac{\partial}{\partial x_0} + \gamma_0\frac{\partial}{\partial x_1} + \ldots, \tag{2.15}$$

and the bathymetry is a function of the long spatial scale $\tilde{h} = \tilde{h}(x_1)$. Then, we expand η and φ in asymptotic series of ε_0

$$\eta(x,t) \to \sum_{k=0}^{\infty}\varepsilon_0^k\eta_k(t, x_0, x_1, \ldots), \qquad \varphi(x,t) \to \sum_{k=0}^{\infty}\varepsilon_0^k\varphi_k(t, x_0, x_1, \ldots). \tag{2.15a,b}$$

Similar to Johnson (1973), we replace x_0 and t with left- and right-moving coordinates translating with speed $\tilde{c}(x_1)$ dependent on the stretched coordinate x_1:

$$\xi_+ = -t + \int^{x_0}\frac{\mathrm{d}x_0'}{\tilde{c}(\gamma_0 x_0')}, \qquad \xi_- = t + \int^{x_0}\frac{\mathrm{d}x_0'}{\tilde{c}(\gamma_0 x_0')}. \tag{2.16}$$

Then, we replace the derivatives ∂_t and ∂_{x_0} with

$$\frac{\partial}{\partial t} = \frac{\partial}{\partial\xi_-} - \frac{\partial}{\partial\xi_+}, \qquad \frac{\partial}{\partial x_0} = \frac{1}{\tilde{c}}\left(\frac{\partial}{\partial\xi_-} + \frac{\partial}{\partial\xi_+}\right). \tag{2.17}$$

Now, we will assume that $\varepsilon_0 \sim P_0 \sim \mu_0 \ll 1$ and follow the standard multiple-scale technique (*e.g.*, Mei *et al.* 2005; Ablowitz 2011). The order-one terms $\mathcal{O}\left(\varepsilon_0^0\right)$ from (2.13) and (2.14) yield wave equations for ϕ_0 and η_0

$$\frac{\partial^2\phi_0}{\partial\xi_+\partial\xi_-} = 0, \qquad \frac{\partial^2\eta_0}{\partial\xi_+\partial\xi_-} = 0, \tag{2.17a,b}$$

with right-moving solutions

$$\varphi_0 = f_0(\xi_+, x_1) \quad \text{and} \quad \eta_0 = \partial_{\xi_+}f_0(\xi_+, x_1), \tag{2.18}$$

propagating with the slowly varying, linear shallow-water phase speed $\tilde{c}(x_1) = \sqrt{\tilde{h}(x_1)}$.

Continuing to $\mathcal{O}(\varepsilon_0)$ of the asymptotic expansion gives

$$\begin{aligned} -\frac{\partial \eta_1}{\partial \xi_+} + \frac{\partial \eta_1}{\partial \xi_-} + \frac{\partial^2 \varphi_1}{\partial \xi_+^2} + 2\frac{\partial^2 \varphi_1}{\partial \xi_+ \partial \xi_-} + \frac{\partial^2 \varphi_1}{\partial \xi_-^2} &= -2\frac{\gamma_0}{\varepsilon_0}\tilde{c}\frac{\partial^2 \varphi_0}{\partial \xi_+ \partial x_1} + \frac{\gamma_0}{\varepsilon_0}\frac{\partial \tilde{c}}{\partial x_1}\frac{\partial \varphi_0}{\partial \xi_+} \\ -\frac{1}{\tilde{c}^2}\eta_0\frac{\partial^2 \varphi_0}{\partial \xi_+^2} - \frac{\gamma_0}{\varepsilon_0}\frac{\dot{\tilde{h}}}{\tilde{c}}\frac{\partial \varphi_0}{\partial \xi_+} &- \frac{1}{\tilde{c}^2}\frac{\partial \eta_0}{\partial \xi_+}\frac{\partial \varphi_0}{\partial \xi_+} + \frac{\mu_0}{\varepsilon_0}\tilde{h}\frac{1}{6}\frac{\partial^4 \varphi_0}{\partial \xi_+^4}, \end{aligned} \tag{2.19}$$

$$\eta_1 - \frac{\partial \varphi_1}{\partial \xi_+} + \frac{\partial \varphi_1}{\partial \xi_-} = -\frac{P_0}{\varepsilon_0}\frac{1}{\tilde{c}}\frac{\partial \eta_0}{\partial \xi_+} - \frac{1}{2}\frac{\mu_0}{\varepsilon_0}\tilde{h}\frac{\partial^3 \varphi_0}{\partial^3 \xi_+} - \frac{1}{2\tilde{c}^2}\left(\frac{\partial \varphi_0}{\partial \xi_+}\right)^2. \tag{2.20}$$

Eliminating η_1 from these equations gives

$$4\frac{\partial^2 \phi_1}{\partial \xi_+ \partial \xi_-} = -2\frac{\gamma_0}{\varepsilon_0}\tilde{c}\frac{\partial \eta_0}{\partial x_1} - \frac{\gamma_0}{\varepsilon_0}\frac{\partial \tilde{c}}{\partial x_1}\eta_0 - 3\frac{1}{\tilde{c}^2}\eta_0\frac{\partial \eta_0}{\partial \xi_+} - \frac{1}{3}\frac{\mu_0}{\varepsilon_0}\tilde{c}^2\frac{\partial^3 \eta_0}{\partial \xi_+^3} - \frac{1}{\tilde{c}}\frac{P_0}{\varepsilon_0}\frac{\partial^2 \eta_0}{\partial \xi_+^2}. \tag{2.21}$$

The left-hand operator $\partial^2/\partial \xi_- \partial \xi_+$ is the same as the $\mathcal{O}(1)$ differential operator (2.17*a*,*b*). Therefore, the right-hand side must vanish to prevent ϕ_1 from developing secular terms. Thus, the right-hand side becomes the variable-coefficient Korteweg–de Vries–Burgers (vKdV–Burgers) equation

$$\frac{\gamma_0}{\varepsilon_0}\tilde{c}\frac{\partial \eta_0}{\partial x_1} + \frac{1}{2}\frac{\gamma_0}{\varepsilon_0}\frac{\partial \tilde{c}}{\partial x_1}\eta_0 + \frac{3}{2}\frac{1}{\tilde{c}^2}\eta_0\frac{\partial \eta_0}{\partial \xi_+} + \frac{1}{6}\frac{\mu_0}{\varepsilon_0}\tilde{c}^2\frac{\partial^3 \eta_0}{\partial \xi_+^3} + \frac{1}{2\tilde{c}}\frac{P_0}{\varepsilon_0}\frac{\partial^2 \eta_0}{\partial \xi_+^2} = 0. \tag{2.22}$$

Finally, multiplying (2.22) by ε, adding the $\mathcal{O}(1)$ differential equation $\partial_{\xi_-}\eta_0 = 0$ derived from (2.17*a*,*b*), and transforming back to the original, non-dimensional variables x and t yields

$$\frac{\partial \eta_0}{\partial t} + c\frac{\partial \eta_0}{\partial x} + \frac{1}{2}\frac{\partial c}{\partial x}\eta_0 + \frac{3}{2}\varepsilon_0\frac{1}{c}\eta_0\frac{\partial \eta_0}{\partial x} + \frac{1}{6}\mu_0 c^5\frac{\partial^3 \eta_0}{\partial x^3} + \frac{1}{2}P_0 c\frac{\partial^2 \eta_0}{\partial x^2} = 0. \tag{2.23}$$

The pressure term $P_0\partial_x^2\eta_0$ functions as a damping, positive viscosity for offshore $P_0 < 0$ wind, making (2.23) a (forward) vKdV–Burgers equation. Conversely, onshore $P_0 > 0$ wind causes a growth-inducing, negative viscosity giving the backward vKdV–Burgers equation. The backward, constant-coefficient KdV–Burgers equation is ill posed in the sense of Hadamard (Hadamard 1902). Though it is possible the backward vKdV–Burgers equation is also ill posed for certain bathymetries $\tilde{h}$, this is irrelevant here owing to the finite time the wave takes takes to reach the beach.

2.5. *Initial conditions*

Our initial condition will be the solitary-wave solutions of the unforced ($P_0 = 0$), flat-bottom KdV equation. These waves balance the KdV equation's nonlinearity $\eta_0\partial_x\eta_0$ and dispersion $\partial_x^3\eta_0$ terms, propagate without changing shape and require that the height H_0 and width L_0 satisfy $H_0L_0^2 =$ constant. Therefore, we now fix the previously unspecified L_0 by choosing $\mu_0 = (3/4)\varepsilon_0$ so L_0 acts like an effective half-width for the solitary wave initial condition (*e.g.*, Mei *et al.* 2005)

$$\eta_0 = \operatorname{sech}^2(x), \tag{2.24}$$

While the unforced KdV equation also possesses periodic solutions called cnoidal waves, we only consider solitary waves here.

2.6. *Convective breaking criterion*

The asymptotic assumptions used to derive the vKdV–Burgers equation (2.23) fail when the wave gets too large. Therefore, we require a condition to determine when the simulations should stop. We use a convective "pre-breaking" condition similar to that derived by Brun & Kalisch (2018) for solitary waves on a flat-bottom depending on the wave velocity profile $u(x,t)$ at the surface and the phase speed c. They utilized the local Froude number $\mathrm{Fr} := \varepsilon_0 u(x,t)/c$, with the ε_0 coming from non-dimensionalization, and defined convective breaking to occur wherever $\max_x(\mathrm{Fr}) = 1$, where $\max_x$ represents the maximum over x. However, when the Froude number approaches the breaking value of unity, our weakly-nonlinear asymptotic assumption used to derive the vKdV–Burgers equation are violated. Thus, we instead stop our simulations at the smaller pre-breaking Froude number $\mathrm{Fr}_{\mathrm{pb}} := 1/3$ and define the pre-breaking time t_{pb} as the first time this condition is met:

$$\max_x(\mathrm{Fr}) := \max_x\left(\varepsilon_0 \frac{u(x)}{c_{\mathrm{adi}}}\right) = \mathrm{Fr}_{\mathrm{pb}} := \frac{1}{3}\,. \tag{2.25}$$

Likewise, we define x_{pb} as the location on the wave where $\mathrm{Fr} = \mathrm{Fr}_{\mathrm{pb}}$, which will be very near the wave peak. To calculate Fr, we need to estimate $u(x,t)$ and c.

As the solitary wave propagates on a slope, the wave evolves over time and the phase speed c can be ambiguous. One option is to use the adiabatic approximation derived by (Miles 1979) for unforced solitary waves on very gentle slopes:

$$c_{\mathrm{adi}} = \sqrt{h(x_{\mathrm{peak}})}\left(1 + \frac{\varepsilon_0}{2}\frac{\eta(x_{\mathrm{peak}})}{h(x_{\mathrm{peak}})}\right), \tag{2.26}$$

with x_{peak} the location of the wave peak. Alternatively, Derakhti *et al.* (2020) used large eddy simulations to numerically investigate unforced solitary wave breaking on slopes ranging from $\beta = 0.2$ to 0.005 for two different forms of c. They found wave breaking at $\max_x(\mathrm{Fr}) = 0.85$ when using the speed of the numerically-tracked wave peak c_{peak}. However, they also found that the shallow-water approximation $c_{\mathrm{shallow}} = \sqrt{h(x_{\mathrm{peak}}) + \varepsilon_0\eta(x_{\mathrm{peak}})}$ (equivalent to c_{adi} to $\mathcal{O}(\varepsilon_0^2)$) was within 15 % of c_{peak} near breaking. Therefore, we will use (2.26) owing to its simplicity and theoretical foundation. Finally, though these studies all considered unforced solitary waves, our results will show that c_{adi} varies approximately 3 % across pressure magnitudes P_0 for our simulations, so this is a valid approximation.

We now derive the wave velocity profile $u(x,z,t) = \boldsymbol{\nabla}\phi$ by modifying the example of Brun & Kalisch (2018) to include sloping bathymetry and pressure forcing. Combining the vKdV–Burgers equation (2.23) and kinematic boundary condition (2.13) eliminates $\partial_t\eta$ yielding

$$\begin{aligned}\tilde{c}^2\frac{\partial^2\varphi}{\partial x^2} - \tilde{c}\frac{\partial\eta}{\partial x} + \varepsilon_0\left(\eta\frac{\partial^2\varphi}{\partial x^2} + \frac{\partial\eta}{\partial x}\frac{\partial\varphi}{\partial x} - \frac{3}{2}\frac{1}{\tilde{c}}\eta\frac{\partial\eta}{\partial x}\right) - P_0\frac{1}{2}\tilde{c}\frac{\partial^2\eta}{\partial x^2}\\ - \mu_0\left(\frac{1}{6}\tilde{c}^6\frac{\partial^4\varphi}{\partial x^4} + \frac{1}{6}\tilde{c}^5\frac{\partial^3\eta}{\partial x^3}\right) + \gamma_0\left(2\tilde{c}\frac{\partial\tilde{c}}{\partial x_1}\frac{\partial\varphi}{\partial x} - \frac{1}{2}\eta\frac{\partial\tilde{c}}{\partial x_1}\right) = 0\,.\end{aligned} \tag{2.27}$$

Assuming an ansatz

$$\frac{\partial\varphi}{\partial x} = \frac{1}{\tilde{c}}\eta + \varepsilon_0 A(x,t) + \gamma_0 B(x,t) + \mu_0 C(x,t) + P_0 D(x,t) \tag{2.28}$$

$$\implies \frac{\partial^2\varphi}{\partial x^2} = \frac{1}{\tilde{c}}\frac{\partial\eta}{\partial x} + \varepsilon_0\frac{\partial A}{\partial x} + \gamma_0\left(\frac{\partial B}{\partial x} - \frac{1}{\tilde{c}^2}\eta\frac{\partial\tilde{c}}{\partial x_1}\right) + \mu_0\frac{\partial C}{\partial x} + P_0\frac{\partial D}{\partial x}\,, \tag{2.29}$$

we insert (2.28) and (2.29) into (2.27), drop terms of $\mathcal{O}(\varepsilon^2)$ and solve for A, B, C and D

Parameter	Range
ε_0	0.2
μ_0	0.15
$\lvert P/(\rho_w g L_0 \varepsilon_0)\rvert$	0.003125, 0.00625, 0.0125, 0.025, 0.05
β	0.01, 0.015, 0.02, 0.025

Table 1. Range of non-dimensional parameters simulated.

by using the independence of ε_0, γ_0, μ_0 and P_0:

$$A = -\frac{1}{4\tilde{c}^3}\eta^2\,, \qquad B = -\frac{\tilde{c}'}{2\tilde{c}^2}\int_{+\infty}^{x}\eta(x')\,\mathrm{d}x'\,, \qquad C = \frac{\tilde{c}^3}{3}\frac{\partial^2\eta}{\partial x^2}\,, \qquad D = \frac{1}{2\tilde{c}}\frac{\partial\eta}{\partial x}\,. \tag{2.29a–d}$$

Note that A represents the nonlinear contribution, B the effect of shoaling, C the dispersive effect and D the pressure forcing. Finally, the Taylor expansion of $\phi(x,z)$ (2.12) gives the fluid velocity at the surface $u(x,t,z=\varepsilon_0\eta) = \partial_x\phi$ as

$$\begin{aligned} u(x,t) &= \partial_x\varphi - \mu_0\frac{1}{2}\tilde{c}^4\partial_x^3\varphi \\ &= \frac{1}{\tilde{c}}\eta - \varepsilon_0\frac{1}{4\tilde{c}^3}\eta^2 + P_0\frac{1}{2\tilde{c}}\frac{\partial\eta}{\partial x} - \mu_0\frac{\tilde{c}^3}{6}\frac{\partial^2\eta}{\partial x^2} - \gamma_0\frac{\tilde{c}'}{2\tilde{c}^2}\int_{\infty}^{x}\eta(x')\,\mathrm{d}x'\,. \end{aligned} \tag{2.30}$$

Therefore, the Froude number is calculated as

$$\mathrm{Fr} := \frac{\varepsilon u(x,t)}{\sqrt{h(x_{\mathrm{peak}})}}\left(1 + \frac{\varepsilon_0}{2}\frac{\eta(x_{\mathrm{peak}})}{h(x_{\mathrm{peak}})}\right)^{-1}, \tag{2.31}$$

with $u(x,t)$ given by (2.30), and (2.25) defines our pre-breaking condition.

2.7. *Numerics*

The vKdV–Burgers equation (2.23) lacks analytic, solitary-wave-type solutions, so we solve it numerically using a third-order explicit Runge-Kutta adaptive time-stepper with the error controlled by a second-order Runge-Kutta method as implemented in SciPy (Virtanen *et al.* 2020). We discretize the spatial domain using a fourth-order finite difference method on a periodic domain with grid spacing $\mathrm{d}x = 0.05$. We employ adaptive time stepping to keep the relative error below 10^{-6} and the absolute error below 10^{-3} at each step. For all cases, the average time-step is $\Delta t \approx 2\times10^{-3}$. The pressure is initially turned off until the solitary wave is one unit (*i.e.* a half-width L_0) away from the start of the beach slope. The pressure is linearly ramped up to its full value over the time the wave takes to cross a full-width $2L_0$. For numerical stability, we included a biviscosity $\nu_{\mathrm{bi}}\partial_x^4\eta_0$ with $\nu_{\mathrm{bi}} = 1\times10^{-5}$.

We validated the solver against the unforced, flat-bottom analytical solution and had a normalized root-mean-square error of 3.9×10^{-4} after non-dimensional time $t=100$ (longer than the longest simulation) as well as a normalized wave height change of $1-[\max(\eta_0)-\min(\eta_0)]/\left[\max(\eta_0^{(0)})-\min(\eta_0^{(0)})\right] = 2.4\times10^{-4}$. Furthermore, the results were qualitatively consistent with the simulations of Knowles & Yeh (2018) of an unforced solitary wave shoaling on a slope. Finally, the simulation reproduced the finding of Knowles & Yeh (2018) that small waves ($\varepsilon_0 \ll 1$) on weak slopes ($\gamma_0 \ll 1$) yield Green's Law for the wave height $H(x) := \max_t(\eta) \propto h(x)^{1/4}$ (with $\max_t$ the maximum over time t),

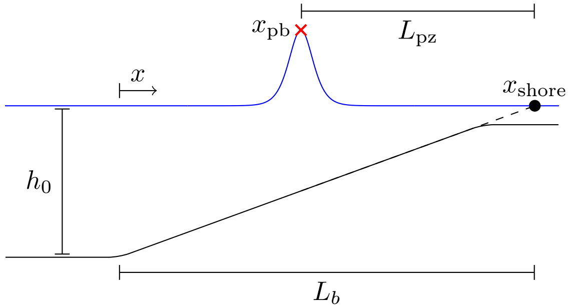

Figure 2. Schematic showing the definition of the pre-breaking zone and shore locations. The blue line represents the water surface and wave profile η at pre-breaking, and the solid black line is the bottom bathymetry $h(x)$. The bathymetry consists of a flat region of depth h_0, a sloping region, and a shallow plateau. The shoreline x_{shore} (black dot) is the location where the bathymetry would intersect the still water level if it had a constant slope (dashed line). The beach width L_b is the distance from the toe of the beach slope to x_{shore}, and the pre-breaking point x_{pb} is the location on the wave where $\text{Fr} = \text{Fr}_{\text{pb}}$, which will be very near the wave peak. The pre-breaking zone width L_{pz} is the distance from x_{pb} to x_{shore}.

while moderate waves ($\varepsilon_0 < 1$) on very weak slopes ($\gamma_0 \lll 1$) give Miles' adiabatic law $H(x) \propto h(x)^{-1}$ (Miles 1983).

The vKdV–Burgers equation (2.22) is determined by two non-dimensional parameter combinations: the pressure term P_0/ε_0 and the shoaling term γ_0/ε_0. Recall that the dispersive term μ_0/ε_0 is a redundancy which we fixed by specifying L_0 (*cf.* § 2.5). We investigate this two-dimensional parameter space by choosing $\varepsilon_0 = 0.2$ and $\mu_0 = 0.15$ and varying the beach slope $\beta = 0.01$ to 0.025 and pressure $P = 0.003\,125$ to 0.05 (*cf.* § 4.1 for a discussion of the size of P). This yields a total of 20 simulations (table 1). Note that (2.22) demonstrates changing $\varepsilon_0 \to \lambda\varepsilon_0$ is equivalent to $\gamma_0 \to \gamma_0/\lambda$ in the wave's co-moving reference frame. Therefore, solutions for waves with different initial heights ε_0 can be generated from our solutions to the vKdV–Burgers equation in the lab frame (2.23) by scaling the height, boosting and adjusting γ_0. Note, the asymptotic expansion assumed $P_0 \sim \varepsilon_0$, or $P/(\rho_w g L_0 \varepsilon_0) \sim 1$, but the pressure values we are using (table 1) are smaller than unity. Nevertheless, multiple-scale expansions are often accurate outside their parameters' validity ranges, and this constraint would be satisfied asymptotically for smaller values of ε_0.

2.8. *Shape statistics*

When stopping the simulations at t_{pb} (§ 2.6), we are interested in determining the wave location x_{pb} at pre-breaking. To estimate how x_{pb} changes, we first calculate the shoreline x_{shore} as the location where the bathymetry would intersect $z = 0$ if it had a constant slope β without our shallow plateau (figure 2). Then, we calculate the pre-breaking zone width as $L_{\text{pz}} := x_{\text{pb}} - x_{\text{shore}}$. For a given beach slope β, we will analyze the change in pre-breaking zone width relative to the unforced case $\Delta L_{\text{pz}} := L_{\text{pz}} - L_{\text{pz}}\big|_{P=0}$ normalized by the unforced pre-breaking zone width $L_{\text{pz}}\big|_{P=0}$. This global statistic $\Delta L_{\text{pz}}/(L_{\text{pz}}\big|_{P=0})$ determines the variance in pre-breaking locations as a fractional change of the pre-breaking zone width.

Additionally, we will investigate four more shape statistics that vary as the wave propagates. The first three are local shape parameters defined at each location x. First, we directly examine the maximum Froude number $\max_t(\mathrm{Fr})$ expressed in (2.31). Second, we investigate the maximum height relative to the local water depth $\max_t(\eta)/h(x)$ at each location x. Third, we consider the maximum slope $\max_t(|\partial\eta/\partial x|)$. Both the relative height and maximum slope contribute to the convective breaking criterion (2.25). Finally, we introduce a global shape parameter, the full width of the wave at half of the wave's maximum (FWHM) $L_W(t)$ normalized by the local water depth $h(x)$. For our unforced KdV solitary wave initial condition (2.24), the FWHM divided by the initial depth is $L_W/h_0 = 2\cosh^{-1}(\sqrt{2})/\sqrt{\mu_0}$. We seek to compare this global shape parameter defined at each point in time t with the local parameters defined at each point in space. Therefore, we define $L_W(x) = L_W(t_{\mathrm{peak}}(x))$ at the time $t_{t_{\mathrm{peak}}}(x)$ when the wave peak passed location x.

3. Results

Now, we use the results of the numerical simulations to investigate the effect of wind on solitary wave shoaling. We will present shape statistics (§ 2.8) for the 20 different runs (table 1) to detail the wave shape changes and pre-breaking behavior across the parameter space. For the remainder of the paper, we will utilize dimensional variables for easier comparison to experiments and observations.

3.1. *Profiles of shoaling solitary waves with wind*

First, we qualitatively investigate the effect of varying pressures P and bathymetric slopes β on solitary-wave shoaling by examining the wave profile η/h_0, normalized by the initial depth h_0, at three different times t (figure 3) corresponding to when the solitary wave first feels the slope ($t = 0$), the time of pre-breaking ($t = t_{\mathrm{pb}}$) and half-way between ($t = t_{\mathrm{pb}}/2$). Note that these $t = 0$ wave profiles (purple in figure 3) are nearly identical to the $\mathrm{sech}^2(x/L_0)$ initial condition (2.24) since the waves have only propagated over a flat bottom (figures 3*g*,*h*) and the pressure has not yet been turned on. Halfway to pre-breaking ($t = t_{\mathrm{pb}}/2$, blue), the solitary wave has grown through shoaling with a steeper front face ($+x$ side) and increased asymmetry for all P and β. At the time of pre-breaking ($t = t_{\mathrm{pb}}$, green) the solitary wave has increased in height, steepened and gained a substantial rear shelf for all P and β. The generation of rear shelves by shoaling solitary waves like those in figure 3 was first calculated by Miles (1979) and results from the mass shed by the sech^2 wave as it narrows. Onshore wind ($P > 0$) reinforces the shoaling-based wave growth and yields relatively narrow peak widths for both β (figures 3*a*,*b*). In contrast, offshore wind ($P < 0$) reduces the wave shoaling but results in wider peak widths (figures 3*a*,*b*). These differences in wave-shoaling result in the offshore-forced ($P < 0$) solitary wave reaching pre-breaking (x_{pb}, $\times$'s in figure 3) farther onshore (shallower water) than the onshore-forced ($P > 0$) solitary wave. Similarly, the larger beach slope ($\beta = 0.025$, figures 3*b*,*d*,*f*) causes waves to reach x_{pb} in less horizontal distance, though they pre-break in shallow water than the milder beach slope ($\beta = 0.015$) waves. At $t = t_{\mathrm{pb}}$, the rear shelf is wider and extends higher up the rear face for offshore winds ($\approx 0.1h_0$ in figure 3*e*) than for onshore winds ($\approx 0.07h_0$ in figure 3*a*). As the control case, the unforced ($P = 0$) solitary wave has x_{pb} located between the onshore and offshore wind cases with an intermediate rear shelf. Finally, the milder slope ($\beta = 0.015$) has a sharper, more pronounced rear shelf while the steeper slope ($\beta = 0.025$) has a more gently sloping rear shelf.

We next investigate the impact of onshore (figures 4*a*,*c*,*e*) and offshore (figures 4*b*,*d*,*f*) wind on shoaling waves' slopes $\partial_x\eta$ and wave velocity profiles $u/\sqrt{gh_0}$. The wave slope

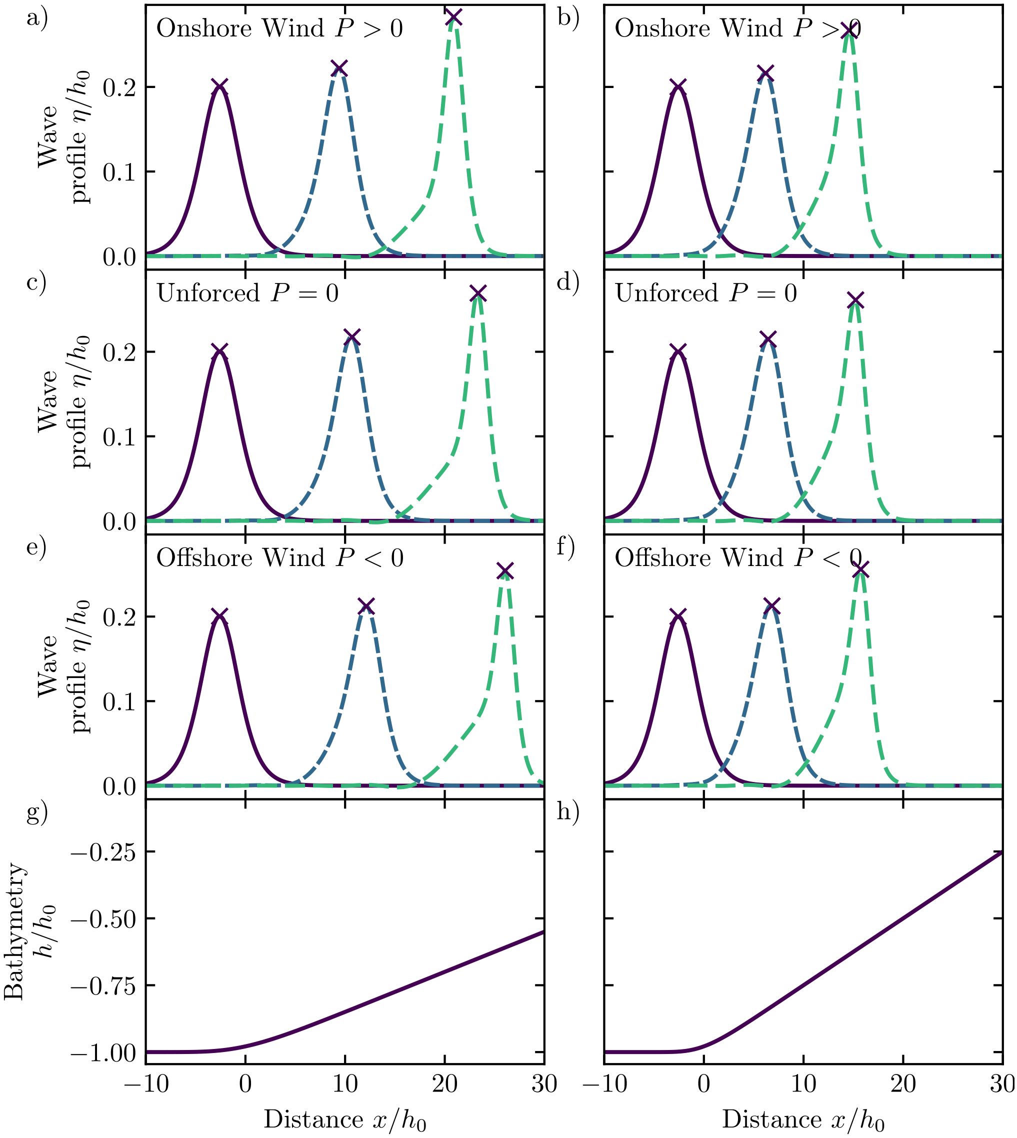

Figure 3. Shoaling solitary-wave η evolution under (a,b) onshore $P > 0$, (c,d) unforced $P = 0$ and (e,f) offshore $P < 0$ wind-induced surface pressure versus non-dimensional distance x/h_0 as the wave propagates up the (g,h) planar bathymetry. The profile times shown depend on the Froude number (2.31) and therefore vary between the panels. The first profile (purple) occurs when the peak is located at $x = -L_0$ where the pressure begins turning on, and the time is defined so $t = 0$ here. The last profile (green) occurs when the convective pre-breaking condition $\max_x(\mathrm{Fr}) = \mathrm{Fr}_{\mathrm{pb}} = 1/3$ is met (*cf.* § 2.6), and the middle profile (blue) occurs at a time halfway between the first and last profiles. Both columns have $\varepsilon_0 = 0.2$ and $\mu_0 = 0.15$, and the left-column forced cases (a,e) have $|P/(\rho_w g L_0 \varepsilon_0)| = 0.05$ and $\beta = 0.015$ while the right-column forced cases (b,f) use $|P/(\rho_w g L_0 \varepsilon_0)| = 0.025$ and $\beta = 0.025$. The $\times$'s denote the locations with the highest Froude number (2.31), and the $\times$'s on the last profiles (green) are the pre-breaking locations x_{pb}. We only display a subset of the full spatial domain.

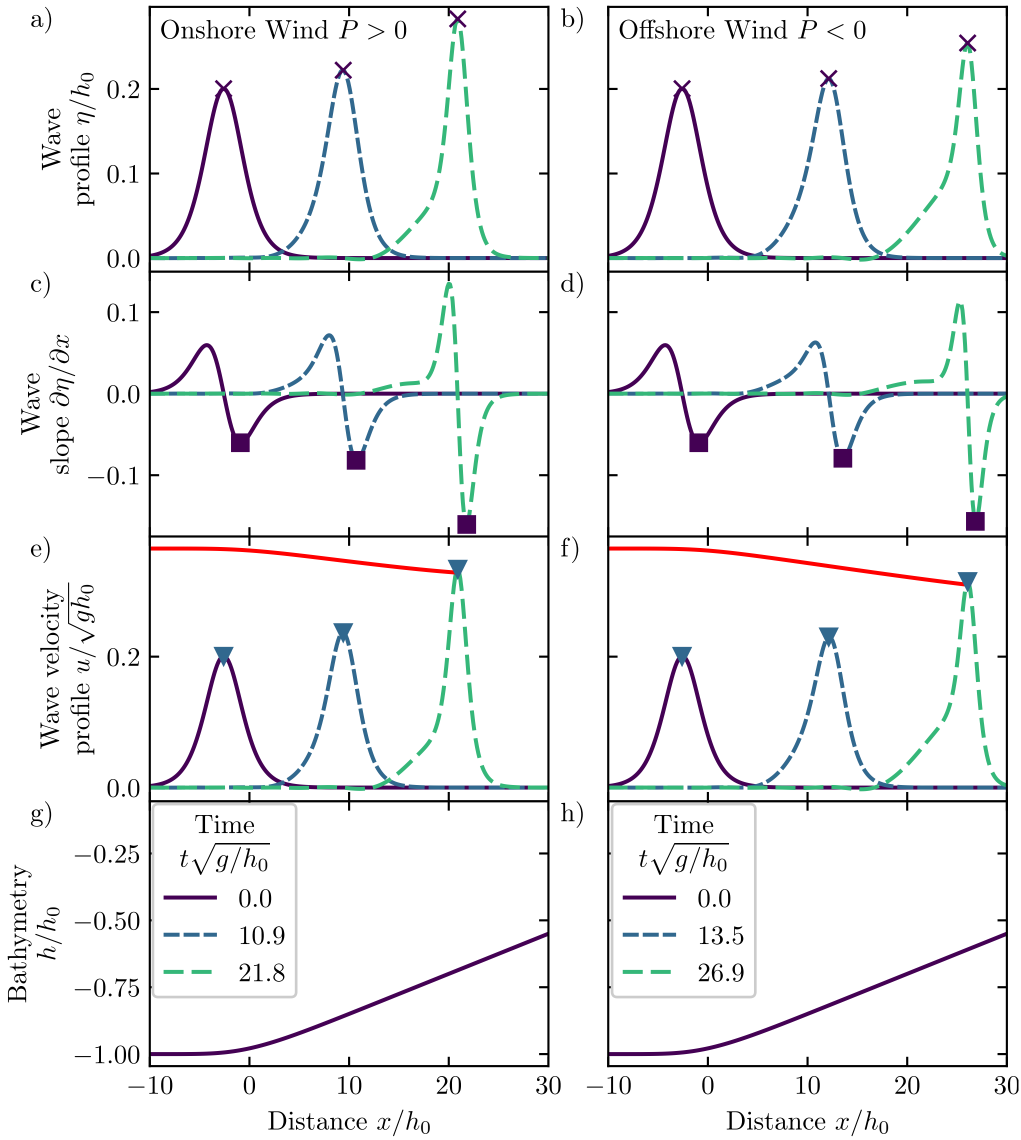

Figure 4. Shoaling solitary-wave (a,b) non-dimensional profile η/h_0, (c,d) slope $\partial\eta/\partial x$ (e,f) and non-dimensional wave velocity profile $u/\sqrt{gh_0}$ under (a,c,e) onshore and (b,d,f) offshore wind-induced surface pressure as the wave propagates up the (g,h) planar bathymetry. Values are shown versus non-dimensional distance x/h_0 for $\varepsilon_0 = 0.2$, $\mu_0 = 0.15$, $|P/(\rho_w g L_0 \varepsilon_0)| = 0.05$, $\beta = 0.015$ and non-dimensional times $t\sqrt{gh}/L_0$ indicated in the legends. The red lines in (e,f) represent the phase speed c_{adi} (2.26) at each location multiplied by the pre-breaking Froude number $\mathrm{Fr}_{\mathrm{pb}} = 1/3$. The $\times$'s denote the locations with the highest Froude number, and the $\times$'s on the last (green) profiles are the pre-breaking locations x_{pb}. The squares are the locations of the maximum slope magnitude $|\partial\eta/\partial x|$, and the upside-down triangles represent the locations of the maximum wave velocity profile. We only display a subset of the full spatial domain.

(figures 4c,d) highlights the shoaling- and wind-induced shape changes by accentuating the front-rear asymmetry. At $t = 0$ (purple figures 4a,b), the wave slope has odd-parity about the peak. However, as the wave propagates onshore, both the front and rear face steepen, though the front face steepens more dramatically. The influence of the wind is most noticeable in three aspects: the offshore-forced wave ($P = -0.05$, figure 4b) is 10 % smaller than the onshore forced wave ($P = 0.05$, figure 4a); the offshore-forced rear-face wave slope (figure 4d) is 15 % smaller than the onshore-forced wave slope (figure 4c), though the front-face slope is only 2 % smaller; and the trailing shelf's slope extends further behind the offshore-forced wave ($\approx 8h_0$, figure 4d) than the onshore-forced wave ($\approx 5h_0$, figure 4c). The wave velocity profile $u/\sqrt{gh_0}$ ((2.30), figures 4e,f) nearly mirrors the wave profile (figures 4a,b), as is expected given that $u \propto \eta$ to leading order (2.30). Finally, the phase speed c_{adi} (red, (2.26)) decreases as the wave shoals which enhances convective pre-breaking, though c_{adi} only varies 3 % between onshore and offshore wind. Note, in figures 4(e,f), c_{adi} is multiplied by $\mathrm{Fr}_{\mathrm{pb}} = 1/3$ so that the intersection of the red curve with the wave velocity profile occurs at x_{pb}, the location of pre-breaking.

3.2. *Shape statistics with shoaling and variations of pre-breaking zone width with wind*

Building on the previous qualitative descriptions of the wave profile, slope and wave velocity profile, we also quantify the change in the shoaling wave's shape parameters for onshore and offshore P (figure 5). First, we consider the maximum Froude number $\max_t(\mathrm{Fr})$ as a function of non-dimensional position x/h_0 (figure 5a). In the flat region ($x < 0$), the maximum Froude number is $\max_t(\mathrm{Fr}) = 0.1818$, and it increases as the waves shoal to the pre-breaking value $\max_t(\mathrm{Fr}) = \mathrm{Fr}_{\mathrm{pb}} = 1/3$ (light gray line). The wind has a significant impact on the location of pre-breaking x_{pb}, with onshore wind (red) causing the Froude number to increase faster and x_{pb} to occur farther offshore than offshore wind (blue) does. This can also be seen in figures 4(e,f), where the maximum velocities $u/\sqrt{gh_0}$ (upside-down triangles), which are proportional to $\max_t(\mathrm{Fr})$, are growing faster for the onshore wind (figure 4e) than the offshore wind (figure 4f). Notably, at a fixed location x/h_0, the $\max_x(\mathrm{Fr})$ varies substantially (*e.g.* 0.25 to 0.30 at $x/h_0 = 20$). In addition, we consider the maximum height $\max_t(\eta)$ at a fixed location and normalized by the local water depth $h(x)$ (figure 5b). For all pressures P, the solitary wave increases in height, but the onshore wind enhances this growth while the offshore wind partially suppresses the growth. Again, this is apparent in the evolution of the maximums $\eta(x_{\mathrm{peak}})/h_0$ in figure 3, with the peak locations x_{peak} closely approximated by the $\times$'s marking the location of maximum Fr. Since $\mathrm{Fr} \propto \eta$ to leading order, the relative height at pre-breaking is approximately 0.41 for all P (figure 5b) with offshore-forced wave slightly larger (1 %) than onshore-forced waves.

Figure 5(c) shows the evolution of the maximum wave slope magnitude $\max_t |\partial_x \eta|$, corresponding to the front face's slope (figures 4c,d). Like the relative height (figure 5b), the steepness is enhanced by onshore wind $P > 0$, suppressed for offshore wind $P < 0$ and approaches nearly the same pre-breaking value of 0.14 for all wind speeds, being only 1 % larger for offshore winds than onshore winds. Finally, we examine the FWHM L_W, normalized by the local water depth $h(x)$ (figure 5d). While $L_W/h(x)$ decreases from its initial value of 4.55 for all pressure magnitudes, there is significant variation in the pre-breaking value. For our parameters, $L_W/h(x)$ changes nearly 19 % more for onshore wind ($P = 0.05$) than offshore wind ($P = -0.05$) from start to pre-breaking. Figures 4(a,b) show that the rear shelf does not rise to half the wave height, so the FWHM does not incorporate the shelf's width. Instead, the onshore-forced narrowing is occurring in the top region above the shelf. Hence, while the relative height and slope at

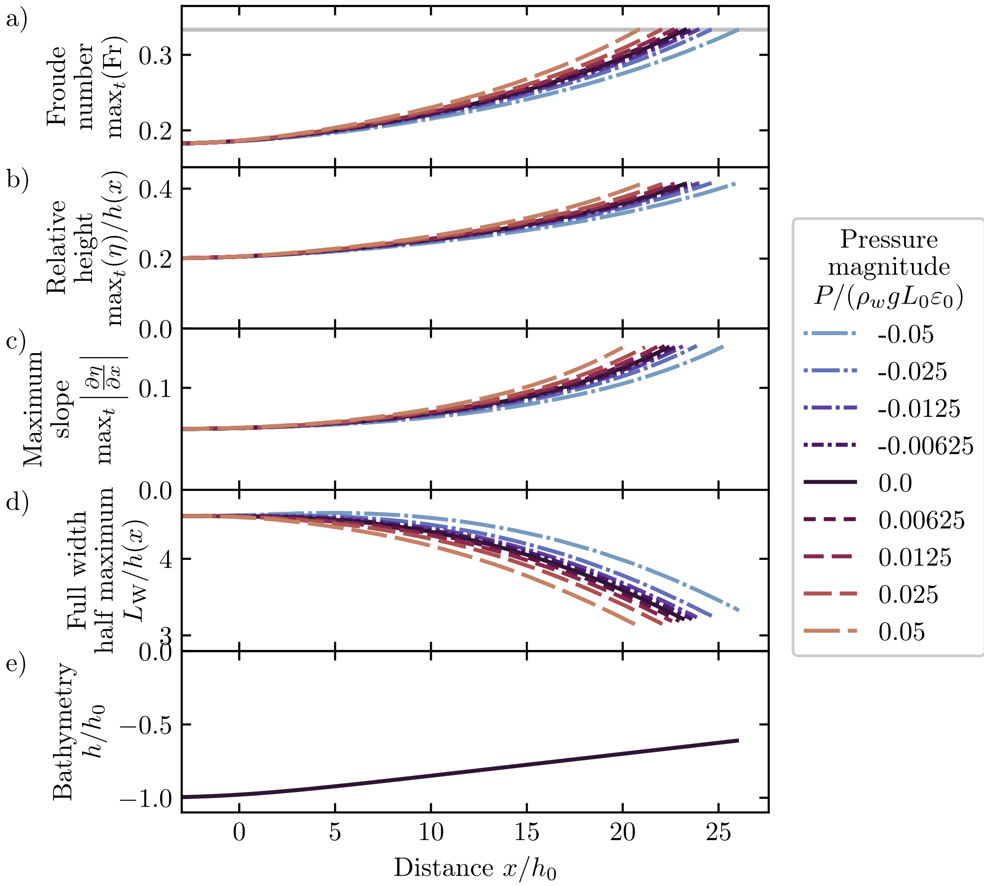

Figure 5. Shoaling solitary-wave shape statistics under onshore and offshore pressure forcing versus non-dimensional distance x/h_0. The (a) Froude number $\max_t(\mathrm{Fr})$ (2.31), (b) maximum height normalized by the local water depth $\max_t(\eta)/h(x)$, (c) maximum slope $\max_t(|\partial\eta/\partial x|)$ and (d) full width at half maximum normalized by the local water depth $L_W/h(x)$ (*cf.* § 2.8) are displayed at each location along the (g) planar bathymetry. Results are shown for $\varepsilon_0 = 0.2$, $\mu_0 = 0.15$, $\beta = 0.015$ and pressure magnitude $|P/(\rho_w g L_0 \varepsilon_0)|$ up to 0.05, as indicated in the legend. The solid black line is the unforced case, $P = 0$. The light gray line on (a) represents the convective pre-breaking Froude number $\mathrm{Fr}_{\mathrm{pb}} = 1/3$ at which the simulations were stopped.

pre-breaking are largely similar for all the wind speeds, the FWHM at pre-breaking is strongly affected by the wind speed indicating wind effects on shoaling shape.

We also investigate the change in the pre-breaking zone width ΔL_{pz} (§ 2.8) as a function of pressure $P/(\rho_w g L_0 \varepsilon_0)$ for four different values of the beach slope β (figure 6). First, ΔL_{pz} is linearly related to the pressure magnitude, and the wind has a larger effect on ΔL_{pz} for smaller beach slopes, with $P/(\rho_w g L_0 \varepsilon_0) = -0.05$ changing the pre-breaking zone width by approximately 5 % for the smallest slope $\beta = 0.01$. This is because the wind has more time to affect the wave before it reaches pre-breaking. This wind-induced change in pre-breaking location is visible in figure 3, where the breakpoint x_{pb} (×'s on green profiles) occurs closer to the shoreline ($+x$ direction) for offshore winds $P < 0$ (figures 3e,f) than for onshore winds $P > 0$ (figures 3a,b). Additionally, we note that for the smallest slope $\beta = 0.01$, the fractional change in pre-breaking zone width $\Delta L_{\mathrm{pz}}/(L_{\mathrm{pz}}|_{P=0})$ is asymmetric

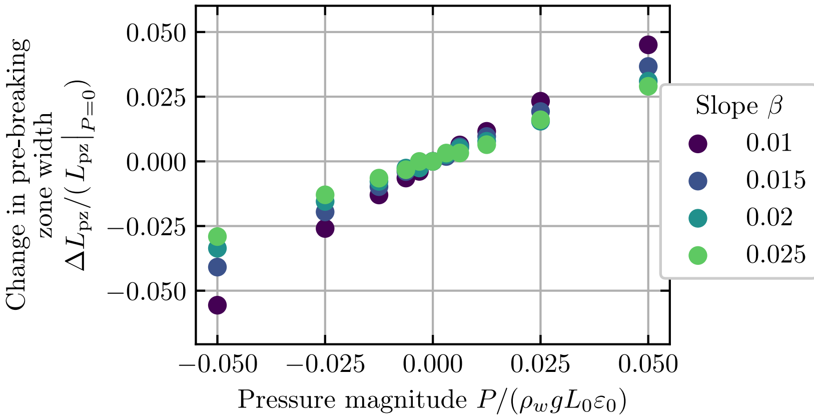

Figure 6. The fractional change in pre-breaking zone width $\Delta L_{\rm pz}$ compared to the unforced case $L_{\rm pz}|_{P=0}$ (*cf.* § 2.8) versus the non-dimensional pressure magnitude $P/(\rho_w g L_0 \varepsilon_0)$. The results are shown for beach slopes $\beta = 0.01$–0.025 as indicated in the legend.

with respect to pressure, with offshore $P/(\rho_w g L_0 \varepsilon_0) = -0.05$ yielding a 23 % larger change than onshore $P/(\rho_w g L_0 \varepsilon_0) = 0.05$ (figure 6).

3.3. *Normalized pre-breaking wave shape changes induced by wind and shoaling*

As figure 5 quantified the shape statistics at pre-breaking for all x, we now directly investigate the effect of pressure P and shoaling β on pre-breaking wave shape by normalizing each pre-breaking wave profile η by its maximum height $\max_x(\eta)$ and aligning the pre-breaking locations $x_{\rm pb}/h_0$ (figure 7). Each solution is dominated by the sech^2 wave centered near $x - x_{\rm pb} = 0$, which becomes taller and narrower as the wave shoals as required by energy conservation (Miles 1979). Furthermore, while the sech^2 component is symmetric in time at a fixed location, it becomes slightly deformed when viewed at a fixed time as the front face moves slower than the rear face (*cf.*, *e.g.*, Newell 1985; Knickerbocker & Newell 1985). We also observe a shelf behind the wave, which Miles (1979) calculated by requiring that the right-moving mass-flux be conserved as the sech^2 narrows and sheds mass. While long-duration calculations of the Miles shelf reveal a nearly horizontal shelf extending far behind the wave (*e.g.*, Knickerbocker & Newell 1980, 1985), our shelf instead slopes gently downward, likely due to insufficient development time and distance.

In figure 7, we plot the pre-breaking wave shape for fixed bottom slope β (figure 7*a*) and fixed pressure magnitude P (figures 7*b*,*c*). For a fixed slope (figure 7*a*), the front wave faces at pre-breaking are qualitatively very similar and match an unforced solitary wave of the same height. However, wind strongly affects the rear shelves as observed in figure 3. The offshore winds (blue) cause the shelf to be thicker and extend higher up the rear wave face than the offshore wind (reds) do, although the shelf intersects $z = 0$ at $(x - x_{\rm pb})/h_0 \approx -10$ for all wind speeds.

We also consider the wave shape at breaking for different values of the beach slope β with a fixed onshore (figure 7*b*) or offshore (figure 7*c*) wind. The rear half of the wave shows that bottom slope β affects the rear shelf differently than pressure $P/(\rho_w g L_0 \varepsilon_0)$ does. While the shelf intersected $z = 0$ at the same location for all wind speeds (figure 7*a*), increasing β causes the intersection point (*i.e.* the base of the shelf) to move forward and closer to the peak. Finally, the offshore wind (figure 7*c*) causes a noticeably larger

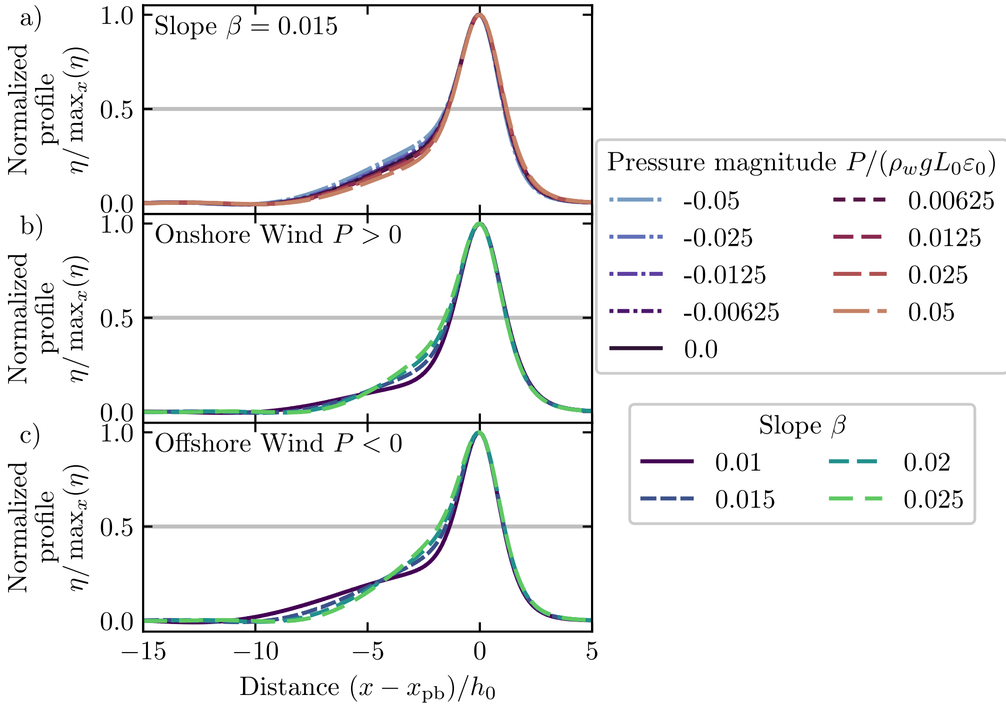

Figure 7. Pre-breaking wave profile $\eta/\max_x(\eta)$ normalized by the maximum height versus non-dimensional position $(x - x_{\text{pb}})/h_0$ relative to the pre-breaking location x_{pb}. All profiles occur at pre-breaking t_{pb} when $\max_x(\text{Fr}) = \text{Fr}_{\text{pb}} = 1/3$ (*cf.* § 2.6) and display different values of the (*a*) pressure magnitude $P/(\rho_w g L_0 \varepsilon_0)$ and the (*b*,*c*) bottom slope β, as indicated in the legend. Results are shown for $\varepsilon_0 = 0.2$, $\mu_0 = 0.15$ and (*a*) slope $\beta = 0.015$, (*b*) onshore $P/(\rho_w g L_0 \varepsilon_0) = 0.05$ or (*c*) offshore $P/(\rho_w g L_0 \varepsilon_0) = -0.05$ pressure magnitude. The light gray line shows where the FWHM is measured.

shelf than the onshore wind (figure 7*b*) for the weakest slope $\beta = 0.01$ (purple), with a similar pattern observed in figure 4(*a*) ($\beta = 0.015$) compared to figure 4(*b*) ($\beta = 0.025$). However, this difference is much smaller for the steeper (green) slopes, implying that stronger shoaling partially suppresses the wind-induced shape change because there is less time for pressure to act prior to pre-breaking.

4. Discussion

4.1. *Wind Speed*

Our derivation in § 2 coupled wind to the wave's motion through the use of a surface pressure (2.5). The resulting vKdV–Burgers equation (2.23) had a wind-induced term dependent on the pressure magnitude constant $P/(\rho_w g L_0 \varepsilon_0)$. We analyzed the evolution and pre-breaking of solitary waves for variable P (§ 3). While the usage of P was the most natural since it is the physical coupling between wind and waves (in the absence of viscous tangential stress), measuring the surface pressure is challenging in field observations or lab experiments (*e.g.*, Donelan *et al.* 2006; Buckley & Veron 2019). Therefore, we also consider the evolution and pre-breaking of the shoaling solitary waves as a function of the wind speed U. Zdyrski & Feddersen (2021) did this by considering a surface pressure acting on a flat-bottom KdV solitary wave initial condition (equivalent to our (2.24))

$\lvert P/(\rho_w gL\varepsilon)\rvert$	h[m]	$U_{\mathrm{onshore}}[\mathrm{m\,s^{-1}}]$	$U_{\mathrm{offshore}}[\mathrm{m\,s^{-1}}]$	h[m]	$U_{\mathrm{onshore}}[\mathrm{m\,s^{-1}}]$	$U_{\mathrm{offshore}}[\mathrm{m\,s^{-1}}]$
0	2.5	4.9	4.9	1	3.1	3.1
0.0031	2.5	8.7	1.2	1	5.5	0.73
0.0063	2.5	10	−0.41	1	6.5	−0.26
0.013	2.5	13	−2.6	1	7.9	−1.7
0.025	2.5	16	−5.8	1	9.9	−3.6
0.050	2.5	20	−10	1	13	−6.5

Table 2. Wind speeds as functions of pressure $P/(\rho_w gL\varepsilon)$ and local depth h for solitary waves (4.1) with $\varepsilon = 0.2$. U_{onshore} corresponds to $P > 0$ and U_{offshore} to $P < 0$. The conversion from $P/(\rho_w gL\varepsilon)$ to U is given in (4.2).

with dimensional form

$$\eta = \varepsilon h \,\mathrm{sech}^2\left(\sqrt{\frac{3\varepsilon}{4}}\frac{x}{h}\right)^2, \tag{4.1}$$

with non-dimensional height $\varepsilon = H/h$ and width $L = 2h/\sqrt{3\varepsilon}$ in water of depth h. They used energy growth rate considerations and a non-separated parameterization by Donelan *et al.* (2006) for periodic, shallow-water waves to approximate the wind speed U as

$$\frac{U}{\sqrt{gh}} = 1 \pm \sqrt{\frac{1}{5}\left|\frac{P}{\rho_w gh\varepsilon}\right|\frac{\rho_w}{\rho_a}\frac{2}{4.91}} = 1 \pm \sqrt{\frac{1}{5}\left|\frac{P}{\rho_w gL\varepsilon}\right|\frac{\rho_w}{\rho_a}\frac{4}{4.91\sqrt{3\varepsilon}}}, \tag{4.2}$$

where U is measured at a height of half the solitary wave's width. Note that the radicand differs by a factor of 2 from Zdyrski & Feddersen (2021) owing to the different definitions of ε. Even though (4.2) was originally applied to flat-bottomed KdV solitary waves (2.24), our assumption that $\gamma = L/L_b \ll 1$ implies that the bathymetry is approximately flat over the wave's width $2L$. Therefore, we use (4.2) to translate between the pressure $P/(\rho_w gL_0\varepsilon_0)$ and the wind speed U at any point on the sloping bathymetry by using the local ε and h and relating the initial pressure to the local pressure $P/(\rho_w gL\varepsilon) = (\varepsilon_0 L_0/\varepsilon L)P/(\rho_w gL_0\varepsilon_0)$.

Table 2 shows the onshore ($P > 0$) and offshore ($P < 0$) wind speeds corresponding to the pressures used in our simulations for two representative depths h. It shows that the pressure magnitudes in our simulations correspond to physically reasonable wind speeds, with onshore U from $3.1\,\mathrm{m\,s^{-1}}$ to $13\,\mathrm{m\,s^{-1}}$ for water 1 m deep or $4.9\,\mathrm{m\,s^{-1}}$ to $20\,\mathrm{m\,s^{-1}}$ for water 2.5 m deep. Notice that unforced waves with $P = 0$ correspond to a wind speed matching the wave phase speed $U = c$, with c approximately the linear shallow-water phase speed $c \approx \sqrt{gh}$. In particular, this means that onshore $P > 0$ and offshore $P < 0$ winds with the same pressure magnitude $|P|$ will have different wind speed magnitudes $|U|$. Additionally, note that keeping P fixed implies that the wind speed U changes as the wave shoals. This is mostly due to the decrease in the phase speed $c \propto \sqrt{gh}$, with higher-order effects coming from the ε and L dependence of the radicand in (4.2). Finally, note that as the wave shoals and ε increases, the height at which the wind speed is measured $z = L/2 = h/\sqrt{3\varepsilon}$ decreases.

We now re-examine our results regarding the pre-breaking zone width (figure 6) in terms of the wind speed $U/\sqrt{gh(x)}$ using (4.2). In addition to changing the abscissa of the plot (figure 8), we also modify the definition of the change in pre-breaking zone width $\Delta L_{\mathrm{pz}} := L_{\mathrm{pz}} - L_{\mathrm{pz}}\big|_{U=0}$ by comparing and normalizing each pre-breaking zone width to the $U = 0$ case rather than the $P = 0$ case. This transformation changes the initially straight lines of figure 6 into approximate pairs of upward- and downward-facing $\sqrt{\Delta L_{\mathrm{pz}}}$

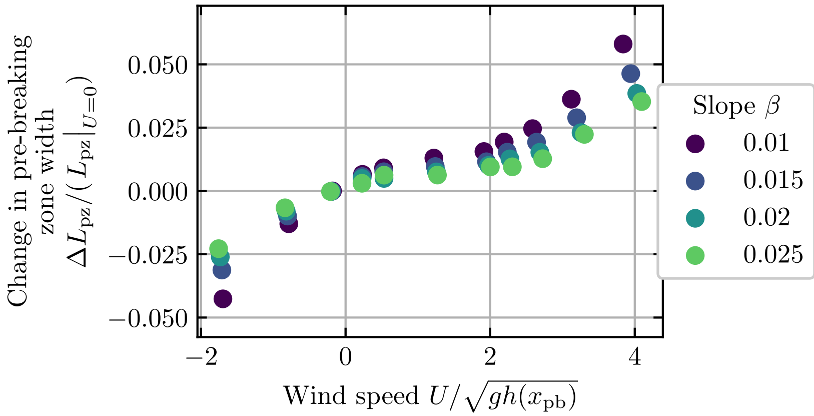

Figure 8. The fractional change in pre-breaking zone width $\varDelta L_{\mathrm{pz}}$ compared to the unforced case $L_{\mathrm{pz}}\big|_{U=0}$ (*cf.* § 2.8) versus the non-dimensional wind speed $U/\sqrt{gh(x_{\mathrm{pb}})}$ normalized by the local, shallow-water phase speed $\sqrt{gh(x_{\mathrm{pb}})}$ and evaluated at a height of half the solitary wave width L. The results are shown for beach slopes $\beta = 0.01$–0.025.

curves shifted to the right by one unit (figure 8). Furthermore, we see that $\varDelta L_{\mathrm{pz}}$ is now much flatter for onshore winds ($U > 0$) than for equal magnitude offshore winds ($U < 0$). This is due to the inflection point of the unforced case ($P = 0$) being shifted to the right at $U/\sqrt{gh} = 1$.

4.2. *Isolating the Effect of Wind*

For no wind ($P = 0$), solitary wave shoaling is well-understood to generate a rear shelf (Miles 1979). The variation in the rear shelf's thickness with P (figure 7) is reminiscent of the variability in the wind-generated bound, dispersive, and decaying tails of flat-bottom solitary waves (Zdyrski & Feddersen 2021). Additionally, Zdyrski & Feddersen (2021) showed that flat-bottom, wind-generated tails are analogous to the dispersive tails of KdV solutions with non-solitary-wave initial conditions (*e.g.* Mei *et al.* 2005). Both the rear shelf and wind-generated tail can be viewed as weak perturbations to the KdV equation by transforming the non-dimensional vKdV–Burgers equation (2.22) into a constant-coefficient, perturbed KdV equation by defining $\nu := (3/2)\eta_0/\tilde{h}^2$, and $\tau := \int \tilde{c}\,\mathrm{d}x_1\,\varepsilon_0/(6\gamma_0)$:

$$\frac{\partial \nu}{\partial \tau} + 6\eta_0 \frac{\partial \nu}{\partial \xi_+} + \frac{\partial^3 \nu}{\partial \xi_+^3} = -\frac{9}{4}\frac{\gamma_0}{\varepsilon_0}\frac{1}{\tilde{h}}\frac{\partial \tilde{h}}{\partial x_1}\nu - 3\frac{1}{\tilde{c}^3}\frac{P_0}{\sqrt{\varepsilon_0\mu_0}}\frac{\partial^2 \nu}{\partial \xi_+^2}\,. \tag{4.3}$$

The first term on the right-hand-side (RHS) is the shoaling term which leads to the rear shelf (Miles 1979), and the second term is the wind-induced Burgers term (Zdyrski & Feddersen 2021). With non-dimensional $P_0 = 0$, (4.3) reduces to the perturbed KdV equation for a gently sloping bottom (*e.g.* Newell 1985). Although our derivation assumed all terms in (4.3) were the same order, $|P_0|/\varepsilon_0 = 0$ to 0.05 and $\gamma_0/\varepsilon_0 = \beta\sqrt{4/(3\varepsilon^3)} =$ 0.1 to 0.3 were smaller than unity, so the RHS terms are weak perturbations to the KdV equation and its sech^2 solitary-wave solution.

Reverting back to dimensional variables, we isolate the effect of wind by separating out the sech^2 solitary wave and the Miles rear shelf using the unforced $P = 0$ normalized profiles to represent shoaling and rear-shelf generation. We define a normalized tail ζ as

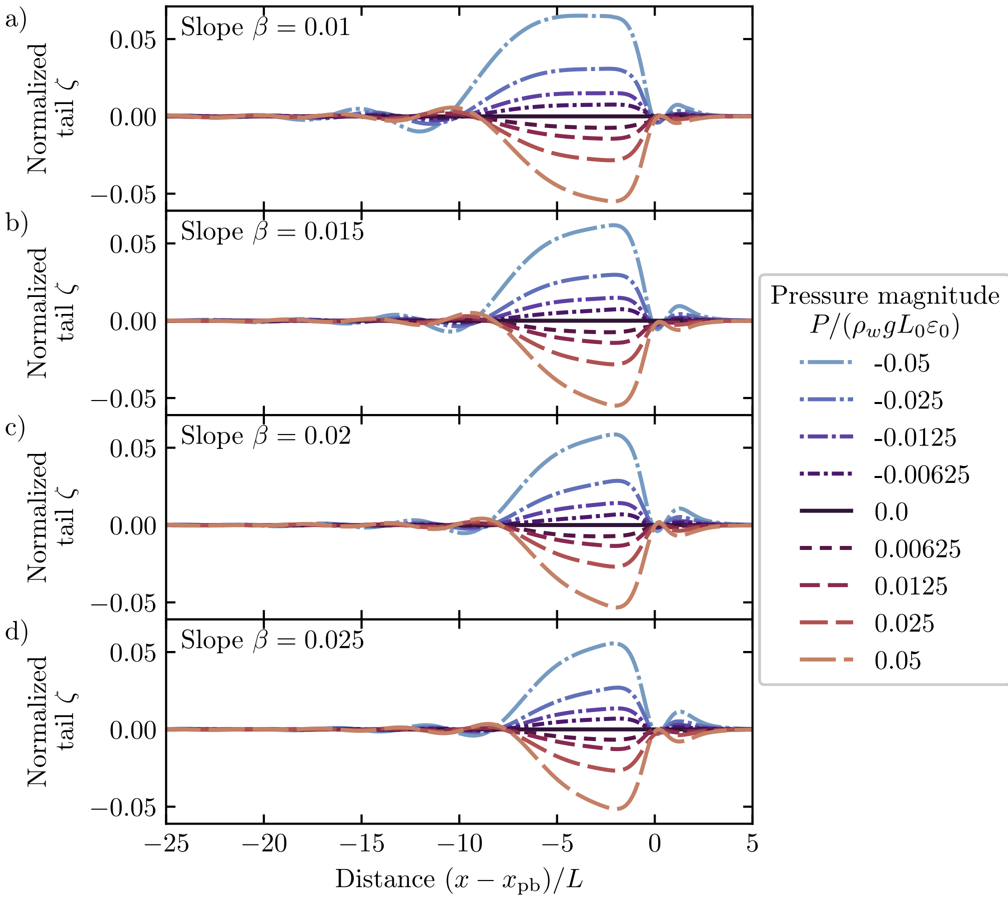

Figure 9. Normalized tail ζ (4.4) versus non-dimensional position $(x - x_{\mathrm{pb}})/L$ relative to the pre-breaking location x_{pb}. The wave profile is normalized by the maximum height $\max_x(\eta)$, and the spatial coordinate $(x - x_{\mathrm{pb}})$ is normalized by the wave width L ((4.5)). All profiles occur at pre-breaking $\max_x(\mathrm{Fr}) = \mathrm{Fr}_{\mathrm{pb}} = 1/3$ (*cf.* § 2.6) and are displayed for bottom slopes β of (a) 0.01, (b) 0.015, (c) 0.02, (d) and 0.025. Results are shown for $\varepsilon_0 = 0.2$, $\mu_0 = 0.15$ and pressure magnitude $|P/(\rho_w g L_0 \varepsilon_0)|$ up to 0.05, as indicated in the legend. The solid black line is the unforced case, $P = 0$, and is zero by definition.

the difference between the forced and unforced $P = 0$ normalized profiles of figure 7:

$$\zeta \coloneqq \frac{\eta}{\max_x(\eta)} - \left(\frac{\eta}{\max_x(\eta)}\right)\bigg|_{P=0}. \tag{4.4}$$

For constant depth, the height H and width L of unforced, sech^2 solitary waves always satisfy $HL^2 = \text{const}$. Since our numerical results (*e.g.* figure 7) are dominated by the sech^2 solitary wave profile, scaling the wave profile by H requires that we scale the spatial coordinate by $L \propto 1/\sqrt{H}$ to respect this symmetry and enable comparison of waves with different heights. We replace $h \to h(x_{\mathrm{peak}})$ in the expression for the flat bottom solitary wave width L (4.1) to yield the wave width for a slowly-varying depth as

$$L = h(x_{\mathrm{peak}})\sqrt{\frac{4h(x_{\mathrm{peak}})}{3H}}. \tag{4.5}$$

We normalize the spatial coordinate as x/L to compare the normalized tails ζ in figure 9.

We show the normalized tail ζ versus $(x - x_{\mathrm{pb}})/L$ for different pressure P and bottom slope β in figure 9. First, increasing the pressure magnitude $|P|$ increases the tail's amplitude and wavelength. For example, the wavelength with $\beta = 0.01$ is approximately $5L$ for $P/(\rho_w g L_0 \varepsilon_0) = -0.025$ and $7.5L$ for $P/(\rho_w g L_0 \varepsilon_0) = -0.05$. This amplitude increase is expected, as higher pressures put more energy into the tail, causing growth. Additionally, increasing the bottom slope β decreases the shelf's width and the tail's amplitude without noticeably changing its wavelength. We can explain the narrower shelf and smaller amplitude by recognizing that larger β's cause the wave to reach pre-breaking (when these profiles are compared) earlier, decreasing the time over which the wind (tail) and shoaling (shelf) act. The wavelength's independence of the beach slope β also implies that the width L of the solitary wave sets the tail's wavelength. Additionally, we note that onshore ($P > 0$) and offshore ($P < 0$) winds change the polarity of the tail, consistent with Zdyrski & Feddersen (2021). Lastly, wind-induces a small, bound wave in front of the pre-breaking solitary wave with minimum near $(x - x_{\mathrm{pb}}) = 0$ and extremum near $(x - x_{\mathrm{pb}})/L \approx 2$ of the same polarity as the rear shelf (figure 9), similar to the flat-bottom results of Zdyrski & Feddersen (2021).

Hence, the numerically-calculated wave profiles (figure 7) are a superposition of the sech^2 solitary wave, Miles' shelf (Miles 1979) and a wind-induced bound, dispersive and decaying tail (Zdyrski & Feddersen 2021). Furthermore, this decomposition of the full wave enables us to understand the effects of wind and shoaling from previously studies. The sech^2 solitary wave grows and narrows due to wave shoaling (*e.g.* Miles 1979) and wind-forcing (Zdyrski & Feddersen 2021). Miles' shelf is generated by the mass-flux of the growing wave. The shelf's absence from the normalized tails in figure 9 implies its shape is largely unchanged by the wind, and its amplitude for a given bottom slope β is approximately proportional to the sech^2 solitary wave. And finally, the amplitude and wavelength of the bound, dispersive and decaying tail grow with the sech^2 solitary wave (Zdyrski & Feddersen 2021).

This decomposition relies on the assumption that the tail and shelf are both small compared to the solitary wave and do not influence each other or the solitary wave. This is only possible when the wind-forcing P_0 is weak and the wave width-to-beach width ratio γ_0 is small. Miles (1979) analyzed a vKdV equation requiring the same weak-slope assumption $\gamma_0 \sim \varepsilon_0$, though his adiabatic results required an even smaller $\gamma_0 = \mathcal{O}\big(10^{-2}\big)$ (Knowles & Yeh 2018). The realistic beach widths we utilized yield a $\gamma_0 = 3 \times 10^{-2}$ to 6×10^{-2} somewhat larger than this adiabatic regime, and the γ_0/ε_0 term in (4.3) is not as small as the pressure-forcing term, implying some nonlinear interactions between the shoaling-induced shelf and the sech^2 solitary are possible. For this reason, we subtracted off the unforced solitary wave and shelf rather than approximate them analytically. Nevertheless, the pressure forcing $|P_0|/\varepsilon_0 = 0$ to 0.05 we used was sufficiently small that the weak wind-forcing can be considered to interact linearly, as seen in the clean separation between pressure-induced tail and sech^2 plus shelf in figure 9.

4.3. *Relationship to previous laboratory experiments and models*

Previous laboratory experiments investigated wind's effect on the breaking characteristics of shoaling, periodic waves (*e.g.*, Douglass 1990; King & Baker 1996). Douglass (1990) considered waves with initial height $H_0/h_0 = 0.3$ and initial inverse wavelength $h_0/\lambda_0 = 0.1$ under wind speeds of up to $U/\sqrt{gh_0} = \pm 2.3$ on a beach with slope 0.04 while King & Baker (1996) considered waves with initial height $H_0/h_0 = 0.2$ and initial inverse wavelength $h_0/\lambda_0 = 0.3$ with wind speeds of up to $U/\sqrt{gh_0} = \pm 1.1$ on a beach with slope 0.05. Douglass (1990) measured how wind speed changes the surf zone width for periodic waves. Directly comparing our figure 8 to figure 2 of Douglass (1990), we see many qualitative similarities, including the pre-breaking zone width's flatter response near $U = 0$ and a stronger response for offshore winds ($U < 0$) than the corresponding onshore winds ($U > 0$), with our change roughly four times smaller than theirs. The laboratory studies also found that the relative breaking height $H(x_{\text{break}})/h(x_{\text{break}})$, normalized by the breaking depth, decreased by as much as 40 % for offshore wind speeds of $U/\sqrt{gh(x_{\text{break}})} = 4$ and increased by up to 10 % for onshore wind speeds of $U/\sqrt{gh(x_{\text{break}})} = -2$ compared to the unforced case (*e.g.*, Douglass 1990; King & Baker 1996). By comparison, over those same wind speed ranges of $U/\sqrt{gh(x_{\text{pb}})} = 1 \pm 3$, our simulations found that the relative pre-breaking height $H(x_{\text{pb}})/h(x_{\text{pb}})$ varied by approximately 1 % between onshore and offshore winds (figure 5*b*), with the same polarity as the laboratory experiments. Numerical studies have also investigated the effect of wind on the breaking of shoaling solitary (*e.g.*, Xie 2014) and periodic (*e.g.*, Xie 2017) waves using a RANS k–ε model to simulate both the air and water. Xie (2014) considered solitary waves with initial height $H_0/h_0 = 0.28$ on a beach slope of 0.05 with onshore winds of up to $U/\sqrt{gh_0} = 3$, while Xie (2017) investigated periodic waves with initial height $H_0/h_0 = 0.3175$ and initial inverse wavelength $h_0/\lambda_0 = 0.02$ on a beach slope of 0.029 forced by onshore winds up to $U/\sqrt{gh_0} = 2$. These studies determined that the (absolute) maximum wave heights $\max_t(\eta)/h_0$ increased with increasing onshore wind at each location $x < x_{\text{break}}$, consistent with our findings in figure 5(b). Furthermore, we can infer from their wave profiles at different wind speeds that the breaking depth $h(x_{\text{break}})$ increased for onshore winds compared to offshore winds, again consistent with our findings.

Our results qualitatively agree with prior experimental and numerical results (Douglass 1990; King & Baker 1996; Xie 2014), and the quantitative mismatch can be partly explained by the different non-dimensional parameters. Douglass (1990), Xie (2014) and Xie (2017) all used larger initial waves ($\varepsilon_0 \approx 0.3$), so nonlinear effects were likely more important. All of the laboratory and numerical experiments discussed also used steeper beach slopes. Additionally, while the surf zone width change is roughly four times larger for Douglass (1990) than for our simulations over the same wind speed range, Douglass (1990) investigated waves that were actually breaking. In contrast, we stopped our simulations at pre-breaking $\max_x(\text{Fr}) = \text{Fr}_{\text{pb}} = 1/3$, significantly before actual breaking $\max_x(\text{Fr}) \approx 1$ (*e.g.* Derakhti *et al.* 2020), thus we expect smaller changes to the surf zone width.

5. Conclusion

While shoaling-induced changes to wave shape are well-understood, the interaction of wind-induced and shoaling-induced shape changes has not been extensively studied. Utilizing a Jeffreys-type wind-induced surface pressure, we defined four non-dimensional parameters that controlled our system: the initial wave height ε_0, the inverse wavelength squared μ_0, the pressure strength P_0 and the wave width-to-beach width ratio γ_0. We leveraged these small parameters to reduce the forced, variable-bathymetry Boussinesq equations to a variable-coefficient Korteweg–de Vries–Burgers equation for the wave profile η. We also extended the convective breaking criterion of Brun & Kalisch (2018) to include pressure and shoaling. A third-order Runge-Kutta solver determined the time evolution of a solitary wave initial condition up a planar beach under the influence of onshore and offshore winds. Stopping the simulations at a pre-breaking Froude number of 1/3 revealed that the pre-breaking relative height and maximum slope are largely independent of wind speed, but onshore winds cause a narrowing of the waves. The width of the pre-breaking zone is strongly modulated by wind speed, with offshore wind decreasing the pre-breaking zone width by approximately 5 % for the mildest beach slopes. Investigating the wave shape at pre-breaking revealed that the front of the wave is relatively unchanged and matches an unforced solitary wave, while the rear shelf is strongly affected by wind speed and bottom slope. We isolated the effect of wind from the effect of shoaling and revealed a bound, dispersive and decaying tail similar to wind-induced tails on flat bottoms. By leveraging the relationship between surface pressure P and wind speed U, we directly compared our results to existing experimental and numerical results. We found qualitative agreement in surf width changes and wave height changes, and expect better quantitative agreement as the waves propagate closer to breaking. These results suggest that wind significantly impacts wave breaking, and our simplified model highlights the relevant physics. Future avenues of research could include deriving coupled equations for both the water and air motions to more accurately predict the surface pressure distribution.

Acknowledgements. We are grateful to D.G. Grimes and M.S. Spydell for discussions on this work. Additionally, we thank D.P. Arovas, J.A. McGreevy, P.H. Diamond, and W.R. Young for their invaluable insights and recommendations.

Funding. We thank the National Science Foundation (OCE-1558695) and the Mark Walk Wolfinger Surfzone Processes Research Fund for their support of this work.

Declaration of interests. The authors report no conflict of interest.

REFERENCES

Ablowitz, M. J. 2011 *Nonlinear dispersive waves: asymptotic analysis and solitons*, , vol. 47. Cambridge University Press.

Amick, C. J. & Toland, J. F. 1981 On periodic water-waves and their convergence to solitary waves in the long-wave limit. *Philos. Trans. R. Soc. A* **303** (1481), 633–669.

Beji, S. & Battjes, J. A. 1993 Experimental investigation of wave propagation over a bar. *Coast. Eng.* **19** (1-2), 151–162.

Brun, M. K. & Kalisch, H. 2018 Convective wave breaking in the KdV equation. *Anal. Math. Phys.* **8** (1), 57–75.

Buckley, M. P. & Veron, F. 2019 The turbulent airflow over wind generated surface waves. *Eur. J. Mech. B Fluids* **73**, 132–143.

Derakhti, M., Kirby, J. T., Banner, M. L., Grilli, S. T. & Thomson, J. 2020 A unified breaking onset criterion for surface gravity water waves in arbitrary depth. *J. Geophys. Res* **125** (7), e2019JC015886.

Donelan, M. A., Babanin, A. V., Young, I. R. & Banner, M. L. 2006 Wave-follower field measurements of the wind-input spectral function. part ii: Parameterization of the wind input. *J. Phys. Oceanogr.* **36** (8), 1672–1689.

Douglass, S. L. 1990 Influence of wind on breaking waves. *J. Waterw. Port Coast. Ocean Eng.* **116** (6), 651–663.

Elgar, S. & Guza, R. T. 1985 Observations of bispectra of shoaling surface gravity waves. *J. Fluid Mech.* **161**, 425–448.

Feddersen, F. & Veron, F. 2005 Wind effects on shoaling wave shape. *J. Phys. Oceanogr.* **35** (7), 1223–1228.

Freilich, M. H. & Guza, R. T. 1984 Nonlinear effects on shoaling surface gravity waves. *Philos. Trans. R. Soc. A* **311** (1515), 1–41.

Grilli, S. T., Subramanya, R., Svendsen, I. A. & Veeramony, J. 1994 Shoaling of solitary waves on plane beaches. *J. Waterway Port Coast. Ocean Eng.* **120** (6), 609–628.

Grilli, S. T., Svendsen, I. A. & Subramanya, R. 1997 Breaking criterion and characteristics for solitary waves on slopes. *J. Waterw. Port Coast. Ocean Eng.* **123** (3), 102–112.

Hadamard, J. 1902 Sur les problèmes aux dérivées partielles et leur signification physique. *Princet. Univ. Bull.* pp. 49–52.

Hammack, J. L. & Segur, H. 1974 The Korteweg–de Vries equation and water waves. part 2. comparison with experiments. *J. Fluid Mech.* **65** (2), 289–314.

Hara, T. & Sullivan, P. P. 2015 Wave boundary layer turbulence over surface waves in a strongly forced condition. *J. Phys. Oceanogr.* **45** (3), 868–883.

Hasselmann, K. F., Barnett, T. P., Bouws, E., Carlson, H., Cartwright, D. E., Enke, K., Ewing, J. A., Gienapp, H., Hasselmann, D. E., Kruseman, P. & others 1973 Measurements of wind-wave growth and swell decay during the joint north sea wave project (JONSWAP). *Dtsch. Hydrogr. Z* **8** (12).

Husain, N. T., Hara, T., Buckley, M. P., Yousefi, K., Veron, F. & Sullivan, P. P. 2019 Boundary layer turbulence over surface waves in a strongly forced condition: LES and observation. *J. Phys. Oceanogr.* **49** (8), 1997–2015.

Iribarren, C. R. 1949 Protection des ports. In *XVIIth International Naval Congress (Lisbon, Portugal), 1949*, pp. 31–80.

Jeffreys, H. 1925 On the formation of water waves by wind. *Proc. R. Soc. Lond. A* **107** (742), 189–206.

Johnson, R. S. 1973 On the development of a solitary wave moving over an uneven bottom. *Math. Proc. Camb. Philos. Soc.* **73** (1), 183–203.

King, D. M. & Baker, C. J. 1996 Changes to wave parameters in the surf zone due to wind effects. *J. Hydraul. Res.* **34** (1), 55–76.

Knickerbocker, C. J. & Newell, A. C. 1980 Shelves and the Korteweg–de Vries equation. *J. Fluid Mech.* **98** (4), 803–818.

Knickerbocker, C. J. & Newell, A. C. 1985 Propagation of solitary waves in channels of decreasing depth. *J. Stat. Phys.* **39** (5), 653–674.

Knowles, J. & Yeh, H. 2018 On shoaling of solitary waves. *J. Fluid Mech.* **848**, 1073–1097.

Lara, J. L., Ruju, A. & Losada, I. J. 2011 Reynolds averaged Navier–Stokes modelling of long waves induced by a transient wave group on a beach. *Proc. R. Soc. Lond. A* **467** (2129), 1215–1242.

Leykin, I. A., Donelan, M. A., Mellen, R. H. & McLaughlin, D. J. 1995 Asymmetry of wind waves studied in a laboratory tank. *Nonlinear Process Geophys.* **2** (3/4), 280–289.

Mei, C. C., Stiassnie, M. & Yue, D. K. P. 2005 *Theory and Applications of Ocean Surface Waves: Nonlinear Aspects*. *Advanced Series on Ocean Engineering* 2. World Scientific.

Miles, J. W. 1957 On the generation of surface waves by shear flows. *J. Fluid Mech.* **3** (2), 185–204.

Miles, J. W. 1979 On the Korteweg–de Vries equation for a gradually varying channel. *J. Fluid Mech.* **91** (1), 181–190.

Miles, J. W. 1983 Solitary wave evolution over a gradual slope with turbulent friction. *J. Phys. Oceanogr.* **13** (3), 551–553.

Mostert, W. & Deike, L. 2020 Inertial energy dissipation in shallow-water breaking waves. *J. Fluid Mech.* **890**, A12.

Newell, A. C. 1985 *Solitons in mathematics and physics*. SIAM.

O'Dea, A., Brodie, K. & Elgar, S. 2021 Field observations of the evolution of plunging-wave shapes. *Geophys. Res. Lett.* **48** (16), e2021GL093664.

Phillips, O. M. 1957 On the generation of waves by turbulent wind. *J. Fluid Mech.* **2** (5), 417–445.

Phillips, O. M. & Banner, M. L. 1974 Wave breaking in the presence of wind drift and swell. *J. Fluid Mech.* **66** (4), 625–640.

Plant, W. J. & Wright, J. W. 1977 Growth and equilibrium of short gravity waves in a wind-wave tank. *J. Fluid Mech.* **82** (4), 767–793.

Svendsen, I. A. & Hansen, J. B. 1978 On the deformation of periodic long waves over a gently sloping bottom. *J. Fluid Mech.* **87** (3), 433–448.

Toland, J. F. 1999 *On the symmetry theory for Stokes waves of finite and infinite depth*, *Monographs and Surveys in Applied Mathematics*, vol. 106, pp. 207–217. Chapman and Hall/CRC.

Virtanen, P., Gommers, R., Oliphant, T. E., Haberland, M., Reddy, T., Cournapeau, D., Burovski, E., Peterson, P., Weckesser, W. & others 2020 SciPy 1.0: Fundamental Algorithms for Scientific Computing in Python. *Nature Methods* **17**, 261–272.

Wu, J. 1968 Laboratory studies of wind–wave interactions. *J. Fluid Mech.* **34** (1), 91–111.

XIE, Z. 2014 Numerical modelling of wind effects on breaking solitary waves. *Eur. J. Mech. B Fluids* **43**, 135–147.

XIE, Z. 2017 Numerical modelling of wind effects on breaking waves in the surf zone. *Ocean Dyn.* **67** (10), 1251–1261.

YANG, D., MENEVEAU, C. & SHEN, L. 2013 Dynamic modelling of sea-surface roughness for large-eddy simulation of wind over ocean wavefield. *J. Fluid Mech.* **726**, 62–99.

YANG, Z., DENG, B.-Q. & SHEN, L. 2018 Direct numerical simulation of wind turbulence over breaking waves. *J. Fluid Mech.* **850**, 120–155.

ZDYRSKI, T. & FEDDERSEN, F. 2020 Wind-induced changes to surface gravity wave shape in deep to intermediate water. *J. Fluid Mech.* **903**, A31.

ZDYRSKI, T. & FEDDERSEN, F. 2021 Wind-induced changes to surface gravity wave shape in shallow water. *J. Fluid Mech.* **913**, A27.

ZELT, J. A. 1991 The run-up of nonbreaking and breaking solitary waves. *Coast. Eng.* **15** (3), 205–246.

ZONTA, F., SOLDATI, A. & ONORATO, M. 2015 Growth and spectra of gravity–capillary waves in countercurrent air/water turbulent flow. *J. Fluid Mech.* **777**, 245–259.

ZOU, Q. & CHEN, H. 2017 Wind and current effects on extreme wave formation and breaking. *J. Phys. Oceanogr.* **47** (7), 1817–1841.